Ph.D. Dissertation of Materials Science and Engineering

Subsolidus phase relationships and TFT properties of the transparent semiconducting compositions in the Al$_2$O$_3$-ZnO-SnO$_2$ and GeO$_2$-ZnO-SnO$_2$ ternary systems

Al$_2$O$_3$-ZnO-SnO$_2$ 와 GeO$_2$-ZnO-SnO$_2$ 삼원계에서의 투명 반도체 조성의 Subsolidus 상 관계 및 TFT 특성

Fabruary, 2018

Graduate School of Engineering
Seoul National University
Materials Science and Engineering

Abhishek Kumar Sharma

Subsolidus phase relationships and TFT properties of the transparent semiconducting compositions in the Al_2O_3-ZnO-SnO_2 and GeO_2-ZnO-SnO_2 ternary systems

Advisor Prof. Sang-Im Yoo

Submitting a Ph.D. Dissertation of Material Science and Engineering

February, 2018

Graduate School of Engineering

Seoul National University

Materials Science and Engineering

Abhishek Kumar Sharma

Confirming the Ph.D. Dissertation written by

Abhishek Kumar Sharma

February, 2018

Chair	Ki-Bum Kim		(Seal)
Vice Chair	Sang-Im Yoo		(Seal)
Examiner	Byungwoo Park		(Seal)
Examiner	Chan Park		(Seal)
Examiner	Jaegab Lee		(Seal)

Abstract

Subsolidus phase relationships and TFT properties of the transparent semiconducting compositions in the Al$_2$O$_3$-ZnO-SnO$_2$ and GeO$_2$-ZnO-SnO$_2$ ternary systems

Abhishek Kumar Sharma

Department of Materials Science and Engineering

Graduate School of Engineering

Seoul National University

Active matrix organic light emitting diode (AMOLED) and active matrix liquid crystal diode (AMLCD) require high performance thin film transistors (TFTs) to fulfill the demands of modern display technology. To achieve this goal, transparent oxide semiconductors (TOSs) have been proved to be one of the best candidates among semiconductors because of high mobility and transparency. Due to the high cost and low availability of Indium, an Indium-free low-cost TOS

is desirable which can compete with In-Ga-Zn-O (IGZO) in electrical performance. In this study, we investigated subsolidus phase relationships in the Al_2O_3-ZnO-SnO_2 and GeO_2-ZnO-SnO_2 ternary systems to discover semiconducting compositions which can be used as efficient TOSs in TFT devices.

First, we investigated subsolidus phase relationships in the Al_2O_3–SnO_2–ZnO ternary system at 1200ºC in air. The phases and lattice parameters of samples were analyzed by powder X-ray diffraction (XRD). Only one type of solid solutions was found in this ternary system, which is Al-substituted zinc stannate spinel ternary compounds of $Zn_{2-x}Sn_{1-x}Al_{2x}O_4$-type solid solutions with the solubility limit of $2x \approx 0.045$ at 1200ºC in air. We compared solubility limit of Al in Zn_2SnO_4 with other group IIIA elements such as In and Ga in the periodic table. In comparison with In_2O_3–SnO_2–ZnO and Ga_2O_3–SnO_2–ZnO ternary systems previously reported, the solubility limit of Al^{3+} ($\approx$ 4.5 mol %) in the $Zn_{2-x}Sn_{1-x}Al_{2x}O_4$-type solid solution is much smaller than those of In^{3+} and Ga^{3+} in Zn_2SnO_4 for the substitution of the Sn^{4+} site, where In^{3+} and Ga^{3+} solubility limits are 90 and 100 mol % at 1275ºC and 1250ºC, respectively, in air. The reason for this limited solubility of Al is described in detail. In addition, unlike previous report, no solid solution was found to exist more than 0.5 mol% of Zn^{2+} in Al_2O_3 at 1200°C in air. On the basis of our experimental data, we were able to construct the subsolidus phase diagram of the Al_2O_3–SnO_2–ZnO ternary system at 1200°C in air.

Second, we selected few compositions (T1-6) from this ternary system near Zn_2SnO_4 to prepare RF sputtering target. Thin films were prepared using these targets. Structural, electrical and optical properties of the thin films were investigated in detail. On the basis of these properties, films prepared using target T1, T2 and T3 were selected for active layer in TFT devices. Thin films prepared with these compositions showed amorphous structure with good TFT properties, where $\mu_{Sat} = 5.446$ (cm^2/Vs), SS $= 1.097$V/dec, $V_{th} = 3.95$V and $I_{on}/I_{off} = 5.3 \times 10^5$. These properties are comparable with other Zn-Sn-O based TFTs (Table 1.2).

Third, the subsolidus phase diagram of the GeO_2–ZnO–SnO_2 at 1100ºC in air was constructed by carefully investigating the phase compatibilities in the GeO_2–ZnO–SnO_2 ternary system. For this study, numerous samples of various nominal compositions were prepared by conventional solid state reaction. Two different solid solutions were found in this ternary system at 1100ºC in air. One was a new ternary compounds of $Zn_2Sn_{1-x}Ge_xO_4$–type solid solutions, and the other was the binary compounds of $Sn_{1-y}Ge_yO_2$-type solid solutions, with the solubility limits of $x \approx 0.08$ and $y \approx 0.06$, respectively.

Fourth, we selected two compositions ($Zn_2Sn_{0.95}Ge_{0.05}O_4$ and Zn_2SnO_4) from the Ge-Zn-Sn-O ternary system for the RF sputtering target. Structural, electrical and optical characterizations were performed on the thin films prepared with these targets. On the basis of

those properties, two films were selected for the active layer in TFT devices, one is Ge4 (Ge-doped ZnSn-O) and other ZTO4 (undoped Zn-Sn-O). Enhancement of the TFT characteristics of Zn-Sn-O thin films by trap density reduction due to Ge doping observed. Thin film samples were prepared using RF magnetron sputtering of the single targets composed of $Zn_2Ge_{0.05}Sn_{0.95}O_4$ and Zn_2SnO_4, showed amorphous structure. Ge-doped Zn-Sn-O thin films exhibit much lower carrier concentration ($1.02x10^{13}$ cm^{-3}), high resistivity (35260 Ωcm) with high Hall mobility (17.99 cm^2/Vs) compared to Zn-Sn-O films. The Ge-doped Zn-Sn-O TFT show a superior performance with subthreshold swing of 1.39 V/decade, threshold voltage (V_{th}) of +5 V and I_{on}/I_{off} ratio of 2.5 x10^6. The bulk trap density of Ge-doped Zn-Sn-O film and the trap density at the active layer/gate oxide (SiO_2) interface decreased one order of magnitude to $7.047x10^{18}$ eV^{-1}cm^{-3} and 3.52 x10^{11} eV^{-1}cm^{-2}, respectively. Thus, Ge was confirmed as an effective carrier suppressor and trap reducer in the Zn-Sn-O system with an improved TFT performance.

Keywords: Transparent oxide semiconductors (TOSs), doped–Zn-Sn-O (ZTO), thin film transistors TFTs, solid solubility limit, ternary phase diagram, Al-Zn-Sn-O and Ge-Zn-Sn-O ternary systems, oxygen binder and trap density reduction.

Student number: **2011-31277**

Contents

Chapter 3. Subsolidus phase relationships, structural-optical-electrical and TFT properties of the semiconducting compositions in Al_2O_3-ZnO-SnO_2 ternary system

Chapter 4. Subsolidus phase relationships, structural-optical-electrical and TFT properties of the

List of Tables

List of Figures

Chapter 1. Introduction

1.1 Transparent oxide semiconductors (TOS)

Since the very beginning, in the field of electronic material research, efforts have been made to find better performance devices through technological advancement and/or by materials development and investigations so that they can fulfill the demand of the modern trends. This is how the journey of researchers, which started with Si-based semiconductor-technology reached to transparent oxide semiconductors (TOS). In the midway several classes of semiconductors were discovered, for example compound semiconductors (GaAs, InN, AlN etc.), organic semiconductors (small molecules Alq3, polymer MEH-PPV etc.), Sillicon carbide (SiC) and now transparent oxide semiconductors (TOS: $InGaZnO_\delta$, doped-Zn_2SnO_4 etc). Especially for present display industries TOS's seems to be the most promising candidate. The reasons are: among all semiconductors, TOS's only have transparency in the film form decorated with excellent electrical properties. At present commercial display products with high resolution, such as 4000×2000 pixels, a high frame rate (>240 Hz), and sizes larger than 70 inches requires high performance semiconductors. A variety of display products can be seen in the Fig. 1.1. Comparatively much better electrical performance including high transparency and amorphous structure of TOSs (transparent oxide semiconductors) make them more suitable and promising candidate over Si based SC (semiconductor) for

the application as electrodes and active layer in flat panel displays and other commercial devices at present. In search of these efficient materials, several metal-oxide ternary systems have been studied, for example Ga_2O_3–In_2O_3–SnO_2 [1] , Ga_2O_3–In_2O_3–ZnO [2], and In_2O_3–SnO_2–ZnO [3] [4]. As a result, few compositions like IGZO[5] and doped-ZTO[6] with excellent electrical properties were discovered. Table 1.1 shows a few high performance TOSs-TFTs reported till date. Now the research focus is on Indium free cost efficient TOS materials. It was found that Indium free TOS's like doped ZTO have comparable electrical and optical properties to IGZO and could be a replacement for the same. To enhance the electrical and optical properties of ZTO and make it comparable to IGZO, several efforts have been made using Hf^{4+}, In^{3+}, Ga^{3+}, Si^{4+}, Al^{3+} etc as a doping element in Zn_2SnO_4 [7-12]. Table 1.2 shows various doped-ZTO TFTs and their structural-electrical properties. This resulted in discovery of new semiconducting compositions and compounds. There are few reports which talk about electrical and optical properties of Ge-doped ZnO [13], IGO [14] and IZO [15] TOS materials. It was noticed that Ge^{4+} has never been used as a dopant in Zn_2SnO_4.

Even though TOS's materials are used in the film form, study of bulk phase relations and electrical properties are useful to understand materials fundamental properties. Oxide materials have large range of electrical properties especially conductivity and mobility, which make them extraordinary candidate for semiconductor device application. Many transparent oxide semiconductors (TOSs) have been discovered

and being used in the industries in display panels. ZnO, In_2O_3, Ga_2O_3, Al_2O_3 and SnO_2 are commonly used oxides in TOS and can show excellent electrical properties when properly doped. A well known oxide semiconductor is IGZO [2]. Many oxides like Ga_2O_3 and In_2O_3 in this category are expensive. There have been always efforts to discover new oxide materials which are cost efficient. It was seen that Al^{3+} is used as a dopant in TOS by many research groups [12]. Al_2O_3–SnO_2–ZnO system contains Zn_2SnO_4 which has 2 orders of magnitude less conductivity then ITO's conductivity [16,17].

To replace the expensive In element, several metal oxides have been used as the potential alternative for TCO. Likewise, to find a cost-effective TOS composition compared with IGZO, the Al_2O_3–SnO_2–ZnO and GeO_2–SnO_2–ZnO ternary systems must be very promising. Unfortunately, however the subsolidus phase diagram of these systems have never been reported yet, which is the motivation of this study.

1.2 Electrical, Optical and Structural properties of TOS's

Semiconducting compounds in the bulk phase are generally needed to convert in to the film form so that it can be used in the devices and commercial products. Electrical, optical and structural properties differ a lot in the bulk and film form although having similar stoichiometry or composition. In this section basic electrical, optical and structural properties of the semiconducting thin films will be explained briefly. For the detailed explanation any textbook of solid state physics can be referred.

1.2.1 Electrical properties

1.2.1.1 Effective mass of carriers

It has been experimentally determined that the mass of electron in solid '$m*$' and mass of free electron 'm_0' is not the same. The ratio $m*/m_0$ has the value slightly above or below 1. The difference between the mass of electron in solid '$m*$' and mass of free electron 'm_0' is due to the interactions between drifting electrons and the atoms in crystal. That is why effective mass of an electron is different in the different direction in the lattice. Value of the effective mass is calculated using E-k relation. Energy (E) of the electron varies w.r.t. wave vector (k) following the solution of the Schrödinger equation: $E = \dfrac{\hbar^2 k^2}{2m}$, where $\hbar = h/2\pi$ (h = Planck constant), wave vector $(k) = \pi/a$, and mass of electron (m). The output curves for effective mass and drift velocity of electron can be seen in Fig. 1.2. It shows the variation of drift velocity of electron V_g and effective mass $m*$ as a function of wave vector k according to the following equations. Effective mass $m*$ is inversely proportional to the second derivative of E w.r.t. k. We can see that $m*$ is dependent on the radius of curvature and increases when radius increases. Effective mass of electron is positive and small near the center of the Brillouin Zone and increases with the larger values of k. At the lower part of the diagram in fig 2 (c) band has negative effective mass. It means that the 'particle' under consideration travels in the opposite direction to an applied electric field. This is known as

'electron hole', in other words an empty space of electron. For the high mobility of electrons, semiconducting material must be designed considering solids having small effective mass [18]. A few commonly used oxide semiconductors with their electron effective mass can be seen in Fig. 1.3.

$$V_g = \frac{1}{\hbar}\frac{dE}{dk}$$

$$m^* = \hbar^2 \left(\frac{d^2E}{dk^2}\right)^{-1}$$

1.2.1.2 Mobility

Under an applied electric field how quickly an electron can move through the metal or semiconductor, defines its mobility. It tells that how mobile an electron is within the solid. It is denoted as $\mu = \frac{\upsilon(velocity)}{\mathcal{E}(field)}$ and can be expressed in terms of average scattering time $\left(\mu = \frac{e\overline{\tau}}{m^*}\right)$. Mobility is dependent on several factors because an electron faces several obstacles which travelling within solids. These obstacles limit the velocity of electrons by changing their path of motion. That results in lower conductivity $\left(\sigma = N_e e\mu_e + N_h e\mu_h\right)$, where N_e and N_h are number of electrons and holes, e is charge of electron, μ_e and μ_h are mobility of electron and hole correspondingly. This phenomenon is known as scattering. There are several types of

scattering mechanism and most common will be explained briefly. Two important scattering mechanisms are shown in Fig. 1.4.

a. *Ionized impurity scattering*

Semiconductors are doped with donor and/or acceptors which are basically ionized. They create an electric field around them. The Coulombic force due to the electric field deflects an electron or hole approaching the ionized impurity. This is known as ionized impurity scattering.

b. *Lattice (phonon) scattering*

At the temperature above absolute zero, atoms vibrate and create acoustic waves in the lattice, which are termed as phonon. These phonons interact or collide with electrons or holes and deviate their path of motion.

c. *Grain boundary scattering*

Solid containing two or more phases or amorphous matrix with crystalline particles are prone to grain boundary scattering. It occurs due to different atomic arrangements in different crystal structure. Electrons or holes have different effective mass and velocity in different lattices under same electric field.

Temperature dependence of mobility

At lower temperatures, ionized impurity scattering dominates, while at higher temperatures, phonon scattering dominates, and the actual mobility reaches a maximum at an intermediate temperature. The

dependence of mobility and scattering time for these two mechanisms are expressed by following relations as shown in Fig. 1.5.

Matthiessen's rule

In reality, more than one source of scattering is present, for example both impurities and lattice phonons. "Matthiessen's Rule" gives a good approximation which explains combined effect of different scattering mechanisms on mobility.

$$\frac{1}{\mu} = \frac{1}{\mu_{impurities}} + \frac{1}{\mu_{lattice}} + \frac{1}{\mu_{defects}} + ...$$

1.2.1.3 Conductivity and carrier concentration

Electrical conductivity in oxide semiconductors is due to *intrinsic defects (oxygen vacancies or metal interstitials)* or *extrinsic dopants (typically a higher-valent metal).* Considering both electrons and holes, we can express conductivity as $\left(\sigma = N_e e\mu_e + N_h e\mu_h\right)$. Replacing N_e and N_h results in

$\sigma = 4.84 \times 10^{15} \left(\frac{m^*}{m_0}\right)^{3/2} T^{3/2} e\left(\mu_e + \mu_h\right) \exp\left[-\left(\frac{E_g}{2k_BT}\right)\right]$ where E_g is band

gap and k_B is Boltzmann constant. We can see the dependence of conductivity on carrier concentration N, mobility and effective mass in the above mathematical expressions. We can see that the conductivity and carrier concentration of semiconductors is strongly dependent on temperature. It increases exponentially with the decrease of temperature. Values of conductivity for different materials can be seen in Fig. 1.6. A

typical value of carrier density for semiconductors is below $10^{19} \mathrm{cm}^{-3}$. Above this value materials are generally known as conductors. Carrier density in oxide semiconductors can be controlled by different fabrication techniques. In case of RF magnetron sputtering, ratio of the carrier gas mixture can be changed to achieve the desired value of carrier density by changing the number of oxygen vacancy or metal interstitial in the semiconducting films.

1.2.2 Optical properties

High transparency (>80%) in the visible range of light due to high optical band gap (>3eV) make TOS's very attractive to the display industries. Modern technology demands for the transparent electrode and active layer materials for the thin film transistor (TFT) devices.

1.2.3 Structural properties

As it has been mentioned already that electrical properties like mobility and conductivity is very important to evaluate the performance of the TFT devices. These properties are highly dependent on atomic arrangement or the lattice structure of the semiconducting materials. Presence of grain boundary or multiple phases in the materials are major reasons of scattering which results in lower drift velocity and mobility. Most of the oxide semiconducting or conducting materials carry amorphous structure which is stable at high temperatures too. This is the major reason behind high mobility in TOS's. On the other hand, flexible substrate is becoming favorite for display industries now

days. Because of good mechanical compatibility with flexible substrate, amorphous conducting oxides are the best options.

1.2.4 Thin film transistors (TFTs)

A variety of semiconductors have been used as an active layer in TFTs [19]. Considering all the electro-optical and structural properties of TOS materials, it can be concluded that these materials are very promising over *a*-Si for the TFT application. IGZO is the most common well studied TOS and being used in the industries for TFT in the display panel.

References

1   Edwards, D., Mason, T., Goutenoire, F. & Poeppelmeier, K. A new transparent conducting oxide in the Ga2O3–In2O3–SnO2 system. *Appl. Phys. Lett* **70**, 1706-1708 (1997).

2   Moriga, T., Kammler, D. R., Mason, T. O., Palmer, G. B. & Poeppelmeier, K. R. Electrical and optical properties of transparent conducting homologous compounds in the Indium-Gallium-Zinc Oxide system. *J. Am. Ceram. Soc.* **82**, 2705-2710 (1999).

3   Harvey, S. P., Poeppelmeier, K. R. & Mason, T. O. Subsolidus Phase Relationships in the ZnO-In2O3-SnO2System. *Journal of*

the American Ceramic Society **91**, 3683-3689, doi:10.1111/j.1551-2916.2008.02686.x (2008).

4   Hoel, C. A., Mason, T. O., Gaillard, J.-F. & Poeppelmeier, K. R. Transparent conducting oxides in the ZnO-In2O3-SnO2 system. *Chemistry of Materials* **22**, 3569-3579 (2010).

5   Nomura, K. *et al.* Room-temperature fabrication of transparent flexible thin-film transistors using amorphous oxide semiconductors. *Nature* **432**, 488-492 (2004).

6   Fortunato, E. M. C. *et al.* High mobility indium free amorphous oxide thin film transistors. *Applied Physics Letters* **92**, 222103, doi:10.1063/1.2937473 (2008).

7   Kim, W.-S., Shin, S.-Y., Lee, S.-H., Han, D.-S. & Park, J.-W. High stability of amorphous hafnium–zinc–tin oxide thin film transistors. *Current Applied Physics* **12**, S17-S20, doi:10.1016/j.cap.2012.05.042 (2012).

8   Kwon, J.-Y. *et al.* Investigation of light-induced bias instability in Hf-In-Zn-O thin film transistors: A cation combinatorial approach. *Journal of The Electrochemical Society* **158**, H433-H437 (2011).

9   Fuh, C.-S., Liu, P.-T., Huang, W.-H. & Sze, S. M. Effect of Annealing on Defect Elimination for High Mobility Amorphous Indium-Zinc-Tin-Oxide Thin-Film Transistor. *IEEE Electron Device Letters* **35**, 1103-1105, doi:10.1109/led.2014.2354598 (2014).

10   Jeong, Y., Song, K., Jun, T., Jeong, S. & Moon, J. Effect of gallium content on bias stress stability of solution-deposited Ga–Sn–Zn–O semiconductor transistors. *Thin Solid Films* **519**, 6164-6168, doi:10.1016/j.tsf.2011.04.030 (2011).

11   Wu, C. *et al.* Characterization of amorphous Si-Zn-Sn-O thin films and applications in thin-film transistors. *Applied Physics Letters* **103**, 082109, doi:10.1063/1.4818728 (2013).

12   Bak, J. Y., Yang, S. & Yoon, S. M. Transparent Al–In–Zn–O Oxide semiconducting films with various in composition for thin-film transistor applications. *Ceramics International* **39**, 2561-2566, doi:10.1016/j.ceramint.2012.09.016 (2013).

13   Arita, M., Yamaguchi, M. & Masuda, M. Electrical and optical properties of germanium-doped zinc oxide thin films. *Materials transactions* **45**, 3180-3183 (2004).

14   Nag, A. & Shireen, A. Search for new transparent conductors: Effect of Ge doping on the conductivity of , and. *Solid State*

Communications **150**, 1679-1682,
doi:10.1016/j.ssc.2010.06.025 (2010).

15   Im, Y. J. *et al.* Improvement in the Electrical Performance of
        Ge-Doped InZnO Thin-Film Transistor. *Journal of Nanoscience
        and Nanotechnology* **15**, 7537-7541,
        doi:10.1166/jnn.2015.11156 (2015).

16   Gordon, R. G. Criteria for choosing transparent conductors.
        MRS bulletin **25**, 52-57 (2000).

17   Minami, T. New n-type transparent conducting oxides. *MRS
        Bulletin* **25**, 38-44 (2000).

18   Medvedeva, J. E. Averaging of the electron effective mass in
        multicomponent transparent conducting oxides. *EPL
        (Europhysics Letters)* **78**, 57004 (2007).

19   Fortunato, E., Barquinha, P. & Martins, R. Oxide
        semiconductor thin-film transistors: a review of recent advances.
        Adv Mater **24**, 2945-2986, doi:10.1002/adma.201103228 (2012).

Fig. 1.1. Commercial display products: from wrist watch to wide screen television.
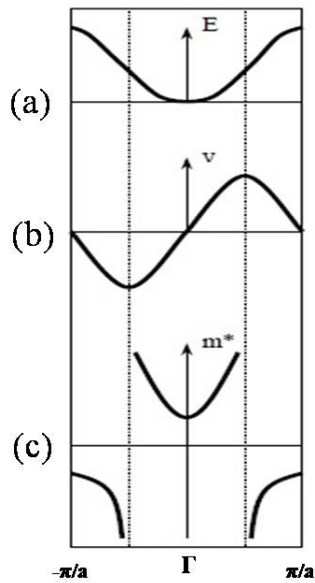
Fig. 1. 2. The dependence of the electron wave function group velocity Vg and the electron effective mass m* on the band energy E(k).
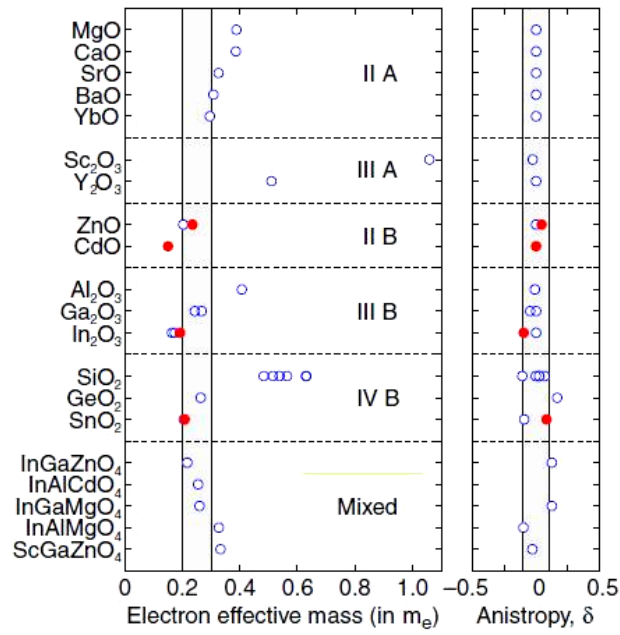
Fig. 1.3. The electron effective mass calculated for different oxide phases.
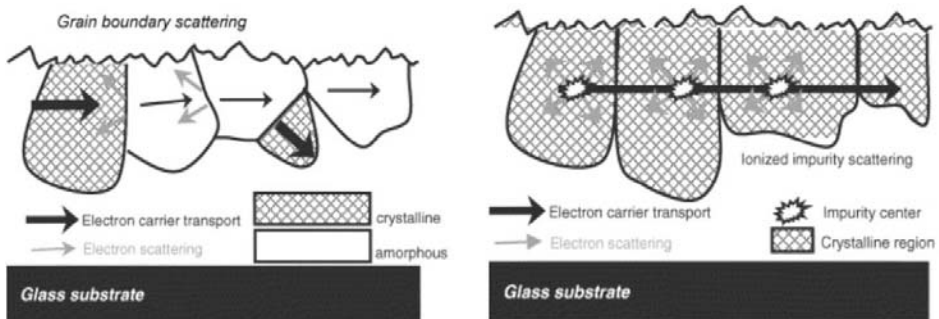
Fig. 1. 4. Schematic diagram showing mechanism of grain boundary and ionized impurity scattering
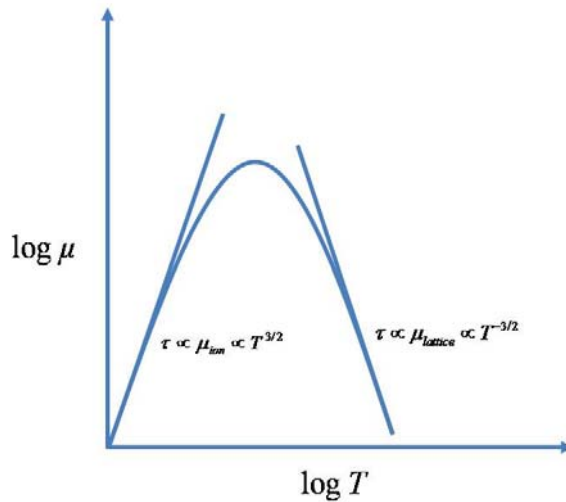
Fig. 1.5. Schematic diagram showing dependence of mobility on temperature.
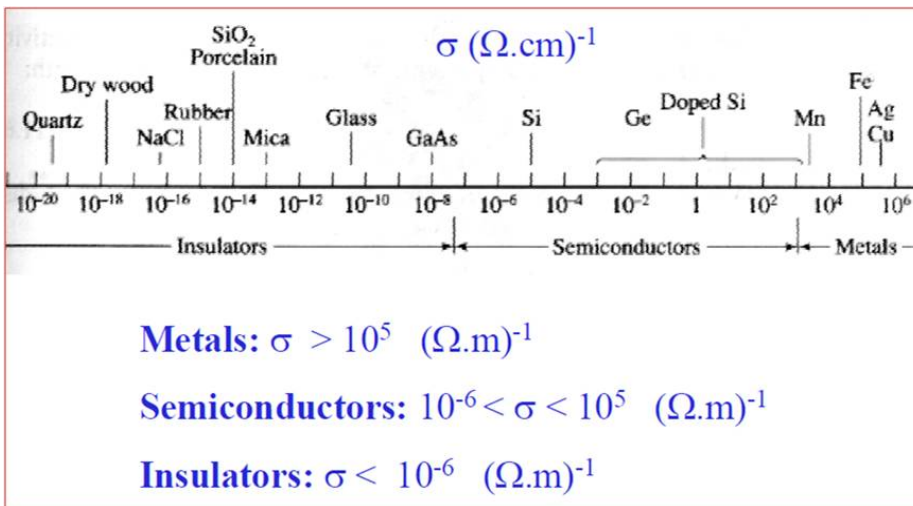
Fig. 1.6. Typical conductivity values for different class of materials.
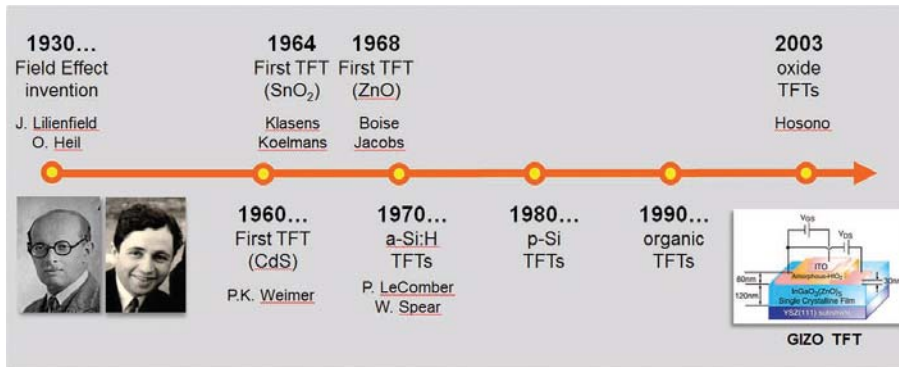
Fig. 1.7 Main landmarks achieved with TFTs (Ref. 19).

Table1.1 High performance TOSs-TFTs reported till date

Common TOS compositions	Structure of the film	Mobility (cm^2/Vs)	Fabrication process	Reference
IGZO	amorphous	12-160	RF sputter	H.W. Zan et al., Advanced Materials, 24 (2012) 3509-3514.
IZO	amorphous	26.5	RF sputter	N. Itagaki et al., physica status solidi (a), 205 (2008) 1915-1919.
IZTO	N/A	52	RF sputter	J.H. Song et al., IEEE Electron Device Letters, 35 (2014) 853-855.
IGO	crystalline	52.6	Solution	Y.G. Kim et al., IEEE Transactions on Electron Devices, 63 (2016) 1078-1084.
ZTO	amorphous	112	solution	Y. Zhang et al.Science China Technological Sciences, 59 (2016) 1407-1412.

16

Table 1.2 . Various doped-ZTO TFTs and their structural-electrical properties.

Doped-ZTO compositions	Structure	Mobility (cm^2/Vs)	Channel dimension (Width / length), μm	Fabrication process	Reference
Al-ZTO (Al$_2$O$_3$, 2 wt % of ZnO)	Amorphous	10.1	40 /20	RF Sputter	D.-H. Cho *et.al*, Applied Physics Letters, 93 (2008) 142111.
ZITO (high In content, >30at%)	Amorphous	3.4-12.4	300/50	RF Sputter	K.J. Saji *et.al*, Journal of The Electrochemical Society, 155 (2008) H390-H395.
Hf-ZTO	Amorphous	5.8	1000/50	RF Sputter	C.-X. Huang *et.al*, Journal of Alloys and Compounds, 681 (2016) 81-87.
Al-ZTO (Al$_2$O$_3$, 3mol%)	Amorphous	< 7	1000/200	RF Sputter	C.-H. Chang *et.al*, Thin Solid Films, 549 (2013) 36-41.
Al-ZTO (0.0025 M Al)	Crystalline	5.41	1500/150	Solution	Y.-G. Lee *et.al*, Electronic Materials Letters, 9 (2013) 719-722.
Si-ZTO (SiO$_2$, 6 mol %)	Amorphous	~1	450/30	RF Sputter	C. Wu *et.al*, Applied Physics Letters, 103 (2013) 082109.
Ga-ZTO:N	Crystalline	4.84	800/200	Solution	B.D. Ahn *et.al*, ACS Appl Mater Interfaces, 6 (2014) 9228-9235.
Nb-ZTO (Nb, 3mol%)	Amorphous	5.32	2000/100	Solution	J.-S. Jeng *et.al*, Journal of Alloys and Compounds, 676 (2016) 86-90.

Chapter 2. Material's design, process and characterization

2.1 Material's design

Many efforts have been made to find criteria to design an efficient TCO material. While designing a material for certain purpose, we must consider their fundamental properties first. In case of oxide semiconductors, one must take the basic electrical properties and electronic configuration under consideration. Most of the TCOs contain heavy post transition metal cations with an electronic configuration of $(n-1)d^{10} ns^0$, where n is the principle quantum number of the cations (n $\geq$ 5). S-orbitals which is spherical and non-directional, exhibit a large spatial spread [1]. This large spatial spread of the metal cations helps in enhancement of electron conduction even in the amorphous oxides via direct overlap of the s-orbitals in the neighboring cations. Because of these reasons, the In_2O_3, Ga_2O_3, ZnO, and SnO_2 have been widely considered as base materials for amorphous semiconductors. Although, these materials are polycrystalline themselves, but in the thin film form with the combination of other oxides like binary or ternary systems, they can form amorphous structure. Uniformity in the crystal structure is very important for the high mobility of the TFT devices [2-4]. Therefore, formation of the amorphous oxides by combining those individual

TCOs has been one of the critical issues in ensuring large-area uniformity.

There are plenty of articles which show the efforts of the researchers who tried to dope these base materials with appropriate metal cations so that they can find a high performance TOS material. These dopants are chosen on the basis of their fundamental electrical properties. We can see the Fig. 1.1 in chapter 1. It gives the value of the effective mass and anisotropy of different oxides, which is very helpful while considering an oxide as dopant.

Another important factor which has to be considered is the valency of the metal cations in the oxide system. ***Kröger–Vink (K-V)*** notation helps in understanding the defect chemistry of the materials as it describes the electric charge and lattice position for point defect species in crystals. With the help of this notation we can understand the carrier generation mechanism in the materials, for example $CdO + SnO_2 + 2In_{In}^{x} \rightarrow Cd_{In}^{''} + Sn_{In}^{\bullet\bullet} + In_2O_3$ where the capital letter stands for the defect or ionic species, the subscript stands for the site, and the superscript stands for effective charge, whether negative (') or positive (●). Using this concept we can select oxides for a multicomponent system. Selection of oxides is based on the valency of metal cation[5].

Ternary systems can be divided into four categories based upon cation charge, namely, divalent (Zn and Cd), trivalent (In, Al and Ga), and tetravalent (Sn and Ge). They can be denoted as 2, 3 and 4. Several combinations are possible with these metal oxides for example (2-2-3),

(2-2-4), (3-3-4), (2-4-4) and (2-3-4) systems. In our study, we chose ZnO-Al$_2$O$_3$-SnO$_2$ (2-3-4) and ZnO-GeO$_2$-SnO$_2$ (2-4-4) type systems [6].

2.2 Process and characterization

2.2.1 Solid state synthesis and thin film fabrication

After selection of the systems mentioned in the previous section, we studied the three binary systems involved in each ternary system. Numerous samples having different nominal compositions in the Al$_2$O$_3$-ZnO-SnO$_2$ and GeO$_2$-ZnO-SnO$_2$ ternary system were prepared by the solid state reaction. The starting materials 99.9% Al$_2$O$_3$, 99.9% GeO$_2$, 99.9% SnO$_2$ and 99.9% ZnO (Kojundo chemical laboratory co. ltd, Japan) were used as the precursors. All the selected compositions from the different part of the ternary phase diagrams for this study were carefully weighed, ball-milled in ethanol with ZrO$_2$ balls for 12 h, dried in oven, and then uniaxially pressed in to pallets. As-pressed pellets were calcined once at 1000°C for 6 h in air. Pallets were ball-milled again for uniform mixing following the same procedure as mentioned above. As pressed pallets were put in to a muffle furnace and sintered at 1200°C in case of Al$_2$O$_3$-ZnO-SnO$_2$ and 1100°C for GeO$_2$-ZnO-SnO$_2$ for 6 h in air. Same process parameters were used to make the RF sputtering target of 50mm diameter. These targets were made using few selected compositions from the phase diagram for the study of the material in thin film form. Using these targets, films were prepared varying different process parameters, like temperature, target- substrate distance, RF power, carrier gas mixture ratio and their pressure in RF

sputtering machine. A schematic diagram of RF sputtering is shown in Fig. 2.1.

2.2.2 TFT device fabrication

After electrical characterization of the thin films, we selected some of the combinations of process parameters for the preparation of active layer in TFT devices. Heavily doped p-type Si-wafer with (100) orientation were used as a substrate for devices. These substrates went through dry oxidation process at 1100°C in a tube furnace to grow an oxide layer (SiO_2) of thickness ~150nm on the Si-wafer. These wafers were further subjected to ultrasonic cleaning in acetone and ethanol sequentially. Semiconducting films with a thickness of 50-100nm were deposited on these substrates and sent to the furnace for annealing at 300°C in low vacuum, nitrogen (N_2), oxygen (O_2) and air in different batches. 'Air' was found to be the best annealing environment for the devices on the basis of the device characteristics. After annealing, 100nm film of Al was deposited using thermal evaporator through a shadow mask having different channel lengths (60, 90, 120, 150, 180 and 200nm) as source-drain (S-D). Heavily doped p-type Si-wafer play the role of gate electrode. These devices were characterized using probe station MS TECH (made in Korea) and Agilent E52808 SMU to get the output and transfer curves. Fig 2.1 shows the schematic of device fabrication process. Several calculations were made using the data of these curves to get the value of field effect mobility (μ)[cm^2/Vs], sub-threshold swing (SS)[V/dec], threshold voltage (V_{th}), I_{on}/I_{off} ratio and contact resistance (Ω) between electrode (S-D) and active layer.

2.2.3 Structural and optical characterization

High-resolution powder X-ray diffractometer (BRUKER, D8 advance) was used for the phase analyses of sintered samples and the thin films prepared through RF sputtering. Lattice parameters were calculated using the PDXL (Integrated X-ray powder diffraction analysis) program. Using these powder XRD data we could construct the ternary phase diagrams. Hitachi (FE-SEM SU-70) scanning electron microscope was used for microstructural characterization and thickness measurement of the thin films. An analytical TEM (JEOL JEM-300F, FEI TecnaiF20) was employed to analyze the cross sectional microstructural characterization of those thin film samples which are prepared by focused ion beam (FIB) milling technique (SMI3050SE).

The optical transmittance of the samples was measured with a SHAIMADZU UV- 2600 UV-VIS spectrophotometer. Absorbance was calculated using transmittance data to obtain optical band-gap of the thin film compositions.

2.2.4 Electrical characterization

2.2.4.1 Resistivity-Temperature (ρ-T)

Temperature dependent resistivity measurement is one of the most fundamental characterization techniques which are employed to identify the basic nature of the materials. Resistivity of insulators, conductors, superconductors and semiconductors give different response to the variation in temperature. In case of semiconductors,

resistivity increases exponentially with the decrease of temperature, as conduction electrons go back to valance band leaving conduction band empty. This measurement was performed on the thin films and sintered pallets under vacuum in a cryostat. These measurements were confirmation of semiconducting properties of the selected oxide compositions from the phase diagram, as they show exponential increase in resistivity at lower temperatures. The ρ/T measurements and E_g (band-gap) calculation were done by the fitting Arrhenius equation in the $\ln(\rho)$-1/T plot using equation

$$\ln \rho = \ln A + \frac{1}{1000} \frac{E_g}{2k} \frac{1000}{T}$$

Where,

$$slope(m) = \frac{1}{1000} \frac{E_g}{2k}$$

2.2.4.2 Hall measurement

Hall measurement is a well known characterization technique based on Hall Effect[7] which tells us the mobility of charge carriers (electrons and holes), resistivity of the material, carrier concentration etc. For the measurement we used ECOPIA Hall effect measurement system (HMS-3300) on thin films prepared by RF sputtering.

References

1   Kwon, J.-Y., Lee, D.-J. & Kim, K.-B. Review paper:
        Transparent amorphous oxide semiconductor thin film transistor.
        Electronic Materials Letters **7**, 1-11, doi:10.1007/s13391-011-
        0301-x (2011).

2   Nomura, K. *et al.* Room-temperature fabrication of transparent
        flexible thin-film transistors using amorphous oxide
        semiconductors. *Nature* **432**, 488-492 (2004).

3   Ellmer, K. Resistivity of polycrystalline zinc oxide films:
        current status and physical limit. *Journal of Physics D: Applied
        Physics* **34**, 3097 (2001).

4   Nomura, K. *et al.* Thin-film transistor fabricated in single-
        crystalline transparent oxide semiconductor. *Science* **300**, 1269-
        1272 (2003).

5   Kröger, F. A. & Vink, H. J. Relations between the
        concentrations of imperfections in solids. *Journal of Physics
        and Chemistry of Solids* **5**, 208-223,
        doi:http://dx.doi.org/10.1016/0022-3697(58)90069-6 (1958).

6   Freeman, A. J., Poeppelmeier, K. R., Mason, T. O., Chang, R. P.
        & Marks, T. J. Chemical and thin-film strategies for new
        transparent conducting oxides. *Mrs Bulletin* **25**, 45-51 (2000).

7   Hall, E. H. On a New Action of the Magnet on Electric Currents.
       American Journal of Mathematics **2**, 287-292,
       doi:10.2307/2369245 (1879).
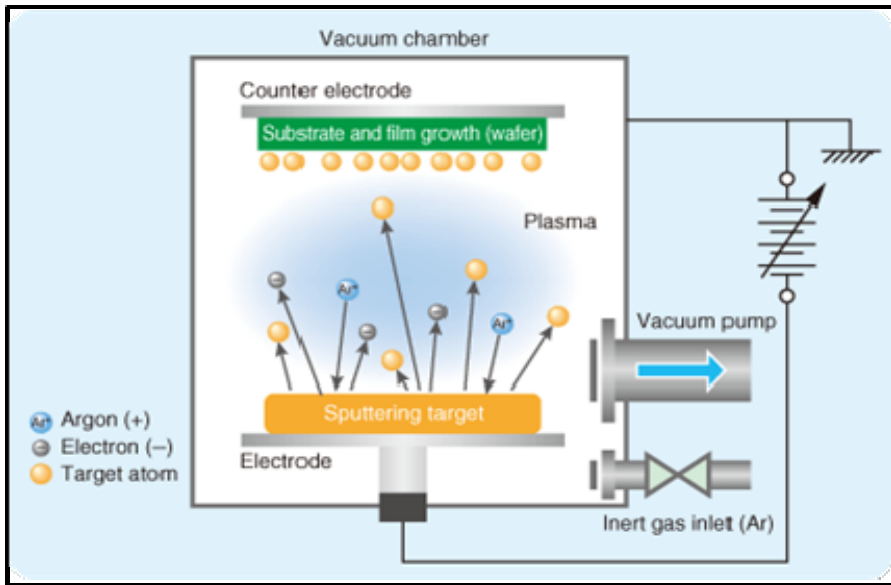
Fig. 2.1 Schematic diagram of RF sputtering (figure from - www.m-system.co.jp)
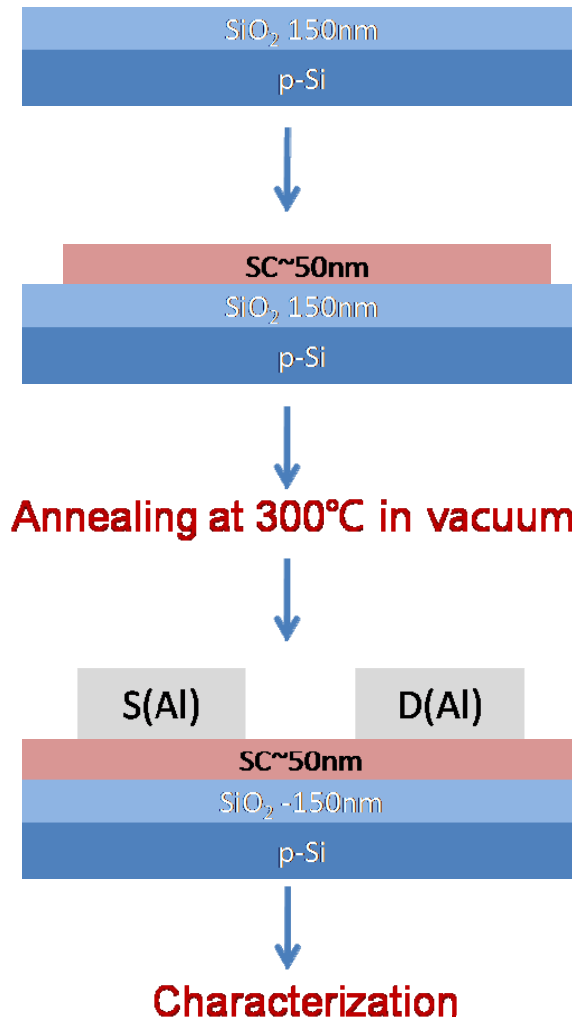
Fig. 2.2 Schematic of the TFT device fabrication process.

Chapter 3. Subsolidus phase relationships, structural-optical-electrical and TFT properties of the semiconducting compositions in Al_2O_3-ZnO-SnO_2 ternary system

3.1 Introduction

The Al_2O_3-ZnO-SnO_2 ternary system involves Al_2O_3-ZnO, ZnO-SnO_2 and Al_2O_3-SnO_2 binary systems [1-3]. Fig 3.1 (a, b and c) show these binary phase diagrams which tell us about the phase relations at 1200°C. The subsolidus Al_2O_3–SnO_2–ZnO ternary phase diagram at 1200°C in air is shown in Fig. 3.2 which is determined on the basis of our experimental data and the information obtained from the previous reports. Table 3.1 shows the phases observed in this study for selected sample compositions. No new ternary compound was found in the phase diagram. Instead, the $Zn_{2-x}Sn_{1-x}Al_{2x}O_4$-type solid solution was discovered to exist between Zn_2SnO_4 and $ZnAl_2O_4$. Each part of the Al_2O_3–SnO_2–ZnO ternary system is described separately below. Some of the compositions from the ternary system were chosen for the study of electrical, optical and TFT characteristics in the thin film form.

3.2 Binary systems

3.2.1 The Al_2O_3–SnO_2 system

Barczak *et al*. [3] reported that the Al_2O_3–SnO_2 binary system contained entirely two phase regions between the end points. It is a

eutectic system which has the eutectic composition of 98% SnO_2 and eutectic temperature of 1620ºC in air, very close to the melting point of SnO_2. Samples were prepared for the nominal compositions near the endpoints of the Al_2O_3–SnO_2 line. All samples were composed of only two phase mixture on their powder XRD patterns, which is in good agreement with previous report [3].

3.2.2 The SnO_2–ZnO system

The SnO_2–ZnO binary system has been reported recently by Mihaiu *et al.* [2]. Only two different binary compounds have been reported in this binary system; spinel Zn_2SnO_4 and ilmenite $ZnSnO_3$. Zn_2SnO_4 (JCPDS Card No. 00-024-1470) is an inverse spinel. The unit cell is cubic, having space group of Fd-3m (227) with lattice parameter, $a = 8.6574$Å. All the Sn^{4+} ions occupy the octahedral sites. Half of the Zn^{2+} ions occupy the tetrahedral sites, and another half octahedral sites. The ilmenite phase of $ZnSnO_3$ could be prepared by an ion exchange method [4,5] and known to be stable only below 600ºC in air. While we tried to synthesize ilmenite $ZnSnO_3$ at 1200ºC in air, this phase was unobtainable, probably due to its thermal instability. Mihaiu *et al.* [2] also reported the existence of three phase mixture (SnO_2, ZnO and Zn_2SnO_4) in the SnO_2–ZnO binary system at the temperature region of 900-1000ºC in air, which definitely violates the Gibbs phase rule.

We are interested in the phase relations at 1200ºC in air where the SnO_2–ZnO system is divided into two sub-systems: SnO_2–Zn_2SnO_4 (0–66.67 mol% ZnO) and Zn_2SnO_4–ZnO (66.67–100 mol% ZnO). The lattice parameters of spinel Zn_2SnO_4 were unchanged while mixing

with the next two end members of SnO_2 and ZnO. There was no evidence for solubility of either of the end members in the spinel Zn_2SnO_4.

3.2.3 The Al_2O_3–ZnO system

The Al_2O_3–ZnO binary system has been first reported by Bunting *et al*. [6], and then reported again by Hansson *et al*. [1]. Both reports show that there exist only three phases in this binary system at 1200ºC in air; corundum (Al_2O_3), spinel ($ZnAl_2O_4$), and zincite (ZnO). $ZnAl_2O_4$ (JCPDS Card No. 00-005-0669) is a normal spinel with lattice parameter a = 8.0848Å and space group Fd-3m (227). Al^{3+} is located at the octahedral site and Zn^{2+} at the tetrahedral site. There exists only one solid solution in this ternary system. According to Hansson *et al*. [1], approximately 2 mol% of ZnO is dissolved by Al_2O_3 from 1250°C to 1695°C, and the solubility of Al_2O_3 in ZnO is 4.7 mol% at 1695°C which rapidly decreases to 0.5 mol% at 1550°C and below with decreasing temperature. It can be seen that $ZnAl_2O_4$ is not a line compound but a solid solution with a significant solubility of Al_2O_3 at higher temperatures in equilibrium with corundum. In the Al_2O_3-ZnO binary phase diagram, they have not reported the solubility limits quantitatively at 1200°C in air. With a careful observation of their phase diagram, approximately ~0.5 mole % of Al_2O_3 was estimated to be dissolved in $ZnAl_2O_4$ at 1200°C in air. However, the existence of $Zn_{1-x}Al_{2+x}O_4$-type solid solution was undetectable in our experimental conditions, and thus we drew the tie line between $ZnAl_2O_4$ and SnO_2. According to their report, 2 mol% of ZnO is dissolved into Al_2O_3 from

1250°C to 1695°C. In order to clarify this point, samples having compositions from 0.5 to 2 mol% of ZnO in Al_2O_3 were prepared and calcined twice at our experimental conditions (1200°C in air). However, no solubility of ZnO in Al_2O_3 was found at this temperature even after twice calcinations, and thus we could draw the tie line between $ZnAl_2O_4$ and SnO_2.

Fig. 4 shows the powder XRD patterns of the samples prepared with various ZnO contents, y from 0.005 to 0.02 mole fraction in $(1-y)Al_2O_3 + yZnO$ binary system. Fig. 5 shows the variation in lattice parameters as a function of ZnO mol% for these samples. The presence of $ZnAl_2O_4$ spinel phase and a negligible change in lattice parameters of Al_2O_3 indicate that there is no solubility down to 0.5 mol% of ZnO in Al_2O_3. We have not prepared samples with lower ZnO contents since it was difficult to maintain accuracy of the compositions by solid state reaction. On the basis of our experimental data, we argue that there is no solubility of ZnO in Al_2O_3 above 0.5 mol% of ZnO at 1200°C in air.

3.3 The Al_2O_3–SnO_2–ZnO system

In this ternary phase diagram, there are three triangular regions as shown in Fig. 1. These are three phase regions. Within all the triangles, the phases contain the endpoint members of the triangle. Region I contains Al_2O_3, SnO_2 and $ZnAl_2O_4$, region II, SnO_2, $Zn_{1.978}Sn_{0.978}Al_{0.045}O_4$ and $ZnAl_2O_4$ and region III, ZnO, $Zn_{1.978}Sn_{0.978}Al_{0.045}O_4$ and $ZnAl_2O_4$. No other phase was found in these regions.

31

Different types of solid solutions have been reported in other ternary systems, containing ZnO, SnO_2 and group III element's oxides, for example, In_2O_3–SnO_2–ZnO [7] and Ga_2O_3–SnO_2–ZnO [8]. Despite of belonging to the same group, IIIA in the periodic table, oxides of In and Ga have different solid solubility with Zn_2SnO_4. Two different solid solutions in the In_2O_3–SnO_2–ZnO system were found: bixbyite solid solution $In_{2-2x}Zn_xSn_xO_3$ (x=0–0.4), and indium substituted zinc stannate spinel, $Zn_{2-x}Sn_{1-x}In_{2x}O_4$ (x = 0–0.45) at 1275ºC. Bixbyite solid solutions were reported as an outstanding TCO compared to spinel solid solutions. On the other hand, in the ternary systems of Ga_2O_3–SnO_2–ZnO, Zn_2SnO_4 and $ZnGa_2O_4$ form a complete solid solution at 1250ºC in air.

In our study, the solubility of Al in Zn_2SnO_4 is limited to ≈ 4.5 mol% at 1200ºC in air, which differs a lot from previous two cases. The $ZnAl_2O_4$ solubility in Zn_2SnO_4 is 100% at 1277ºC but the solid solution starts to decompose while cooling below 1277ºC in air [9]. Our experiments were performed at 1200**º**C in air and it was observed that the Al_2O_3 solubility in Zn_2SnO_4 is around 4.5 mol% after cooling to room temperature. Fig. 2 shows the powder XRD patterns of the compositions which were prepared with different molar ratios of $ZnAl_2O_4$ against Zn_2SnO_4. We can see that there are no $ZnAl_2O_4$ peaks up to 5 mol%. The calculated lattice constants of various samples, including these solid solutions, are represented in Table 2 and plotted in Fig. 3 as a function of Al mole fraction, 2x, indicating that the variation in the lattice parameters is linear up to 2x ~ 0.045 and is insignificant

(< 0.3% reduction of a) for the $Zn_{2-x}Sn_{1-x}Al_{2x}O_4$–type solid solutions, which might be due to a very limited solubility limit. The variation of lattice parameters vs the Al mole fraction 2x in $Zn_{2-x}Sn_{1-x}Al_{2x}O_4$–type solid solutions follows the Vegard's Rule.

Interestingly, the solubility limit of Al (4.5%) in the Zn_2SnO_4 (ZTO) spinel compound is much smaller compared with In (90%) and Ga (100%), which can be understood as the following. In the case of $Zn_{2-x}Sn_{1-x}In_{2x}O_4$-type solid solutions, where In^{3+} substitutes the Sn^{4+} and Zn^{2+} sites equally, the lattice parameter increases from ~8.66Å (at x = 0) to ~8.77Å (at x = 0.45), approximately 1.27%, while the ionic radii of Zn^{2+} (0.740 Å) and Sn^{4+} (0.690 Å) compared with In^{3+}(0.8 Å) is 7.5 and 13.75% smaller, respectively [7,10]. Similarly, in the case of $Zn_{2-x}Sn_{1-x}Ga_{2x}O_4$-type solid solutions, the Ga^{3+} ions substitute the Sn^{4+} and Zn^{2+} sites equally up to x =1, representing a complete substitution for the Sn^{4+} site. The lattice parameter decreases approximately 3.93% from ~8.66Å (at x = 0) to ~8.32Å (at x = 1), while the ionic radii of Zn^{2+} and Sn^{4+} compared with Ga^{3+}(0.62 Å) is 19.35 and 11.29% larger, respectively [8]. In our study, a very limited solid solubility of Al in Zn_2SnO_4 and a small change in the lattice parameters of the Al-substituted Zn_2SnO_4 spinel seem to be reasonable because Al^{3+} (0.535Å) has 6-coordinate ionic radii much smaller than those of Zn^{2+} (0.740 Å) and Sn^{4+} (0.690 Å) with large difference of 38.31 and 28.97%, respectively [10]. Apart from the difference in ionic radii of metal cations, metal-oxygen (M-O) bond length plays very important role in the stability of the structure. The standard M-O distances [9-11] show that the

M-O distances in the octahedral coordination of the spinel structure for In-O, Ga-O, Zn-O, Sn-O and Al-O are approximately 2.16, 2.00, 2.09, 2.09 and 1.91Å, respectively. In comparison with In-O and Ga-O, Al-O has smaller bond length, which can disturb the regularity of the ZnO_4 and MO_6 polyhedra and thus make the structure unstable. Therefore, compared with In and Ga, much smaller the cation size and Al-O bond length seem to responsible for very limited solubility of Al ($0 \leq 2x \leq 0.045$) in $Zn_{2-x}Sn_{1-x}Al_{2x}O_4$–type solid solutions.

The region bounded by $ZnAl_2O_4$, $Zn_{2-x}Sn_{1-x}Al_xO_4$, SnO_2, and Al_2O_3 should be divided into two triangles. There exist two possibilities, one is the tie line between $Zn_{2-x}Sn_{1-x}Al_{2x}O_4$ and Al_2O_3, and the other one is the tie line between $ZnAl_2O_4$ and SnO_2. On the basis of the XRD data of the samples having the nominal compositions on the line connecting $Zn_{2-x}Sn_{1-x}Al_{2x}O_4$ with Al_2O_3, we found that the line contains mixture of three phases except the nominal composition at the point of intersection with the line connecting $ZnAl_2O_4$ with SnO_2. This point contains mixture of two phases: $ZnAl_2O_4$ and SnO_2. Considering these XRD data, we concluded that the region was divided into two triangles by the $ZnAl_2O_4$ - SnO_2 tie line.

The $Zn_{2-x}Sn_{1-x}Al_{2x}O_4$ ternary compounds divide the phase region into two different parts. These two triangular regions are the compatibility regions between two different phases, where one triangle involves ZnO and another SnO_2 in equilibrium with the solid solution $Zn_{2-x}Sn_{1-x}Al_{2x}O_4$ where $2x \approx 0.045$ at 1200ºC in air. These regions are represented in Fig. 1, where several tie lines are connecting the end

members of the ZnO-SnO$_2$ binary system with the ternary solid solutions. The Al^{3+} ion occupy the Sn^{4+} sites in octahedral coordination of O^{2+} ions so that solid solution stability could be maintained in the Zn$_{2-x}$Sn$_{1-x}$Al$_{2x}$O$_4$-type solid solutions, which surely originates from the difference in bond lengths of cation-oxygen [9].

3.4 Structural, electrical, optical and TFT characteristics of Al-doped Zn-Sn-O compositions

Some of the compositions from this ternary system were selected for the further study of their applicability in the semiconducting devices. RF sputtering targets were made of these compositions for thin film preparation. After that, different set of samples in the thin film form were prepared with different set of processing parameters for the characterization of structural, electrical and optical properties. These RF sputtering target compositions are listed below. (Compositions from 1-6 are given a short name T1-T6 respectively for the convenience of writing)

1) $0.95Zn_2SnO_4 + 0.05ZnO$ -----------   (T1)
2) $0.95Zn_2SnO_4 + 0.05SnO_2$ -----------   (T2)
3) $0.9Zn_2SnO_4 + 0.1ZnAl_2O_4$ -----------   (T3)
4) $0.6Zn_{1.98}Al_{0.02}SnO_4 + 0.4SnO_2$ -----------   (T4)
5) $0.4Zn_{1.98}Al_{0.02}SnO_4 + 0.6SnO_2$ -----------   (T5)
6) $Zn_{1.98}Al_{0.02}SnO_4$ -----------   (T6)

3.4.1 Structural, electrical and optical properties

The importance of crystallanity in semiconductors has already been explained in chapter 1 in the context of charge carrier's scattering. The purpose of optimization of the process of film formation and the film composition was to achieve an amorphous structure including better electrical properties. Most of the films prepared using above mentioned targets were having amorphous structure except T4 and T5. Thin films prepared with these two were having SnO_2 crystals in the amorphous matrix. We can see the crystallanity of the thin films having various compositions in Fig 3.7. XRD patterns of the thin films prepared using RF sputtering target of composition T4, T5 and T6 show the presence of SnO_2 crystal in the amorphous matrix. It can be seen clearly that the increase in the SnO_2 content in the target increases crystallanity of the films. So, the films from T1-T3 targets were expected to have amorphous structure and can be used for TFT device fabrication as they are chosen from the surrounding area of the Zn_2SnO_4 with a small variation in the composition in the three different directions. HR TEM was used to understand the phase distribution in the thin films. The TEM micrograph and diffraction patterns confirm the presence of nano size SiO_2 crystals in the amorphous matrix (Fig. 3.11).

Transmittances in the films were measured using UV-Vis-NIR spectrophotometer. It was seen that all the thin film samples were transparent above 80% in the visible range of light. These transmittance data were used for the calculation of absorbance so that we can

calculate the optical band-gap of the thin film compositions. It is necessary that the TOSs films must not have any absorption in the visible range of light and must have band-gap >3.1eV. It was observed that the bang-gap of the compositions were in the range of 3.5-3.8eV which is expected for oxide semiconductors (Fig. 3.12).

Fig. 3.19 shows the transmittance and absorbance of the thin films made from the T1, T2 and T3. Table 3.4 shows the composition of the T1-T3 thin films. These compositions are spotted in the phase diagram (Fig. 3.18). Fig. 3.17 shows the deconvoluted O 1s XP Spectra and relative fraction of O^{2-} associated with vacancies in T1, T2 and T3 films where O_{M-O} = Oxide lattices without oxygen vacancies (~530 eV), V_O = Oxide lattice with oxygen vacancies (~531.5 eV), and O_{M-O} = Hydroxide (~532.0 eV). High Sn content with low defects or traps in T1 and relatively high concentration of oxygen vacancy in T2 and T3 were found. Unassigned peak in T2 may originate from some intermediate compounds like SnO or hydroxides.

Hall measurement data were obtained for most of the films prepared with T1-T6. Fig. 3.8 and 3.9 show the Hall measurement data: mobility, carrier concentration, conductivity and resistivity from the thin films made with the target of composition T5 and T4 respectively at 300ºC for different carrier gas composition $[O_2/(O_2+Ar)]$ during thin film deposition in RF sputtering. With the increase of O_2 %, resistivity increases which arises due to the decrease in O^{2+} vacancies or carrier concentration in the film. Fig. 3.10 shows the variation in mobility,

carrier concentration and resistivity of the films prepared, using T4, T5 and T6 target at different substrate temperatures. As compared to the previous case, temperature variation shows opposite effect. With the increase in temperature, mobility and carrier concentration increases while resistivity decreases for T6-films which are expected, but in T4 and T5-films a random variation of data is seen. It can be seen in the figures that the hall mobility data don't have a continuous increase or decrease with the variable parameters like Ar:O_2 ratio or substrate temperature and show a maximum or minimum for a specific values of the variables. It could be due to the excess of Sn content and the presence of different cationic species in the films which is formed at a particular film deposition condition. These cations affect the movement of the charge carriers by becoming a center of scattering. It has been reported earlier that the oxide films containing Sn as one of the major components, may contain Sn^{2+} with Sn^{4+} cations and become a dominant center of scattering for charge carriers [12].

For the confirmation of the semiconducting behavior of the materials, we performed resistivity-temperature (ρ-T) measurement on the thin films of T4 and T5. We can see in the Fig. 3.13 that the resistivity increases exponentially with the decrease in temperature, which is a fundamental property of the semiconductors. This final characterization of the materials and the results obtained were the motivation for the next stage of this work, which was TFT device fabrication using these materials in active layer.

3.4.2 TFT devices and their characteristics

At first, TFT devices were fabricated using T4 and T5 target materials but they showed very poor characteristics. We can see the transfer curve in the Fig. 3.14 of the devices made using T5 target. It shows very high threshold voltage (V_{th}~-15V), low I_{on}/I_{off} (~10^3-10^4) ratio and very high subthreshold swing SS/dec (>1V) value. Output curves (I_d-V_d) couldn't be obtained for these devices. The reason could be the crystallanity of the films, as they have excess amount of Sn in the form of SnO_2 nano-crystals in the amorphous matrix. Considering this, TFTs were fabricated using T1-T3 sputtering targets, having lower Sn content as compared to T4 and T5 to avoid dual phase in the film.

It has already been mentioned that Zn_2SnO_4 has been studied well and reported as a potential semiconducting composition for the TFT application. To investigate the semiconducting properties in the nearby area in phase diagram three compositions were chosen in three different directions. As compared to Zn_2SnO_4, T1, T2 and T3 are ZnO, SnO_2 and Al_2O_3 rich, respectively. Thin films prepared with these compositions show amorphous structure (Fig. 3.15), which is essential for TOS's.

Electrical characteristics of the TFT devices prepared using T1-T3 are shown in Fig. 3.16. Devices, which belong to T1 showed the best performance among all three, while the characteristics of devices made of T2 were poor. All the device parameters are shown in Table 3.

On the basis of structural and electrical characteristics of the films and devices, we can conclude that the area nearby Zn_2SnO_4 has enough potential to produce amorphous semiconducting compositions with excellent device performance, especially in the direction of $Zn2SnO4 \rightarrow ZnO$ compositions. TFT device characteristics are summarized in Table 3.3.

3. 5 Summery

The subsolidus phase relationships were investigated in the Al_2O_3–SnO_2–ZnO ternary system at 1200°C. There is no new structural compound but a solid solution $Zn_2Sn_{1-x}Al_xO_4$ was found between Zn_2SnO_4 and $ZnAl_2O_4$ join where $x \leq 0.05$. No solid solution between Al_2O_3 and ZnO was found at our experimental condition (1200°C in air), although the work on Al_2O_3-ZnO binary system by Hansson et al. (2004) [1] reported very limited solubility of ZnO in Al_2O_3 and Al_2O_3 in $ZnAl_2O_3$ at and above 1250°C. Compatibilities were identified between ZnO/SnO_2 with the solid solution $Zn_2Sn_{1-x}Al_xO_4$.

References

1   Hansson, R., Hayes, P. C. & Jak, E. Experimental study of
        phase equilibria in the Al-Fe-Zn-O system in air. *Metallurgical
        and Materials Transactions B* **35**, 633-642 (2004).

2   Mihaiu, S. *et al.* Advanced ceramics in the SnO2–ZnO binary
        system. *Ceramics International* **41**, 4936-4945,
        doi:10.1016/j.ceramint.2014.12.056 (2015).

3   Barczak, V. & Insley, R. Phase Equilibria in the System
        Al2O3—SnO2. *Journal of the American Ceramic Society* **45**,
        144-144 (1962).

4   Al-Hinai, M. H., Al-Hinai, A. T. & Dutta, J. Phase
        transformation behavior of zinc metastannates obtained by
        aqueous precipitation at different temperatures. *Journal of
        Materials Science* **49**, 7282-7289 (2014).

5   Gou, H. *et al.* Energetic stability, structural transition, and
        thermodynamic properties of ZnSnO[sub 3]. *Applied Physics
        Letters* **98**, 091914, doi:10.1063/1.3562013 (2011).

6   Bunting, E. Phase equilibria in the system SiO2-ZnO-Al2O3. *J.
        Res. Ntnl. Bur. Stand* **8**, 279-287 (1932).

7   Harvey, S. P., Poeppelmeier, K. R. & Mason, T. O. Subsolidus
        Phase Relationships in the ZnO-In2O3-SnO2System. *Journal of

the American Ceramic Society **91**, 3683-3689, doi:10.1111/j.1551-2916.2008.02686.x (2008).

8   Palmer, G. & Poeppelmeier, K. R. Phase relations, transparency and conductivity in Ga 2 O 3 瑕 SnO 2 瑕 ZnO. *Solid state sciences* **4**, 317-322 (2002).

9   Garbato, A., Garbato, L., Marrocu, P. & Sedda, F. Solid Solubility in Mixed Spinels ZnMIII2O4-Zn2SnO4 (MIII= Al, Ga). *Japanese Journal of Applied Physics* **39**, 134 (2000).

10   Shannon, R. t. Revised effective ionic radii and systematic studies of interatomic distances in halides and chalcogenides. *Acta Crystallographica section A: crystal physics, diffraction, theoretical and general crystallography* **32**, 751-767 (1976).

11   Wei, S.-H. & Zhang, S. First-principles study of cation distribution in eighteen closed-shell A II B 2 III O 4 and A IV B 2 II O 4 spinel oxides. *Physical Review B* **63**, 045112 (2001).

12   Zhu, Q. *et al.* Structural and physical properties of transparent conducting, amorphous Zn-doped SnO2 films. *Journal of Applied Physics* **115**, 033512, doi:10.1063/1.4861378 (2014).
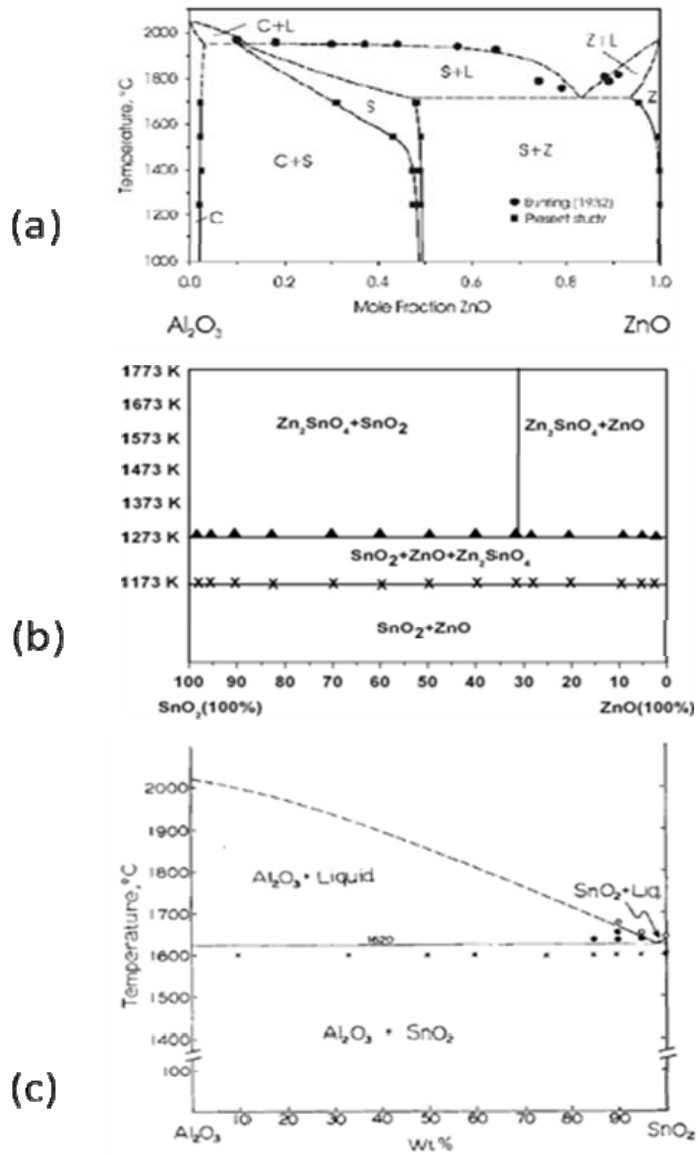
Fig. 3.1 Binary systems of (a) Al_2O_3-ZnO, (b) ZnO-SnO_2 and (c) Al_2O_3-SnO_2 .
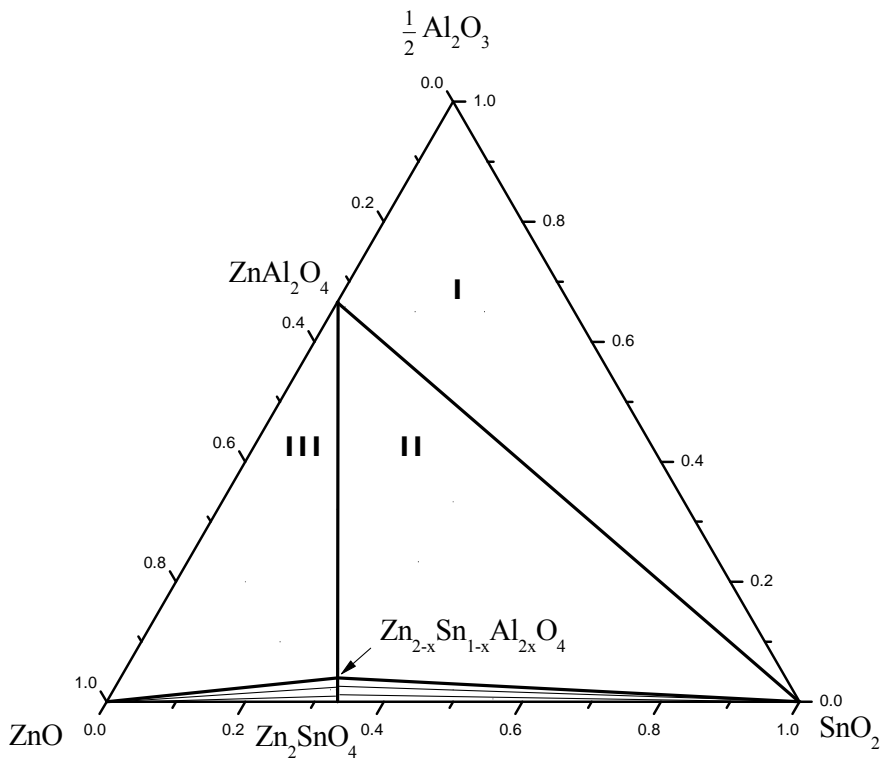
Fig. 3.2 The subsolidus phase diagram for the Al$_2$O$_3$–SnO$_2$–ZnO ternary system at 1200°C in air.

Table 3.1 Samples with various nominal compositions in the Al_2O_3-SnO_2-ZnO ternary system and their phases analyzed by XRD.

Nominal compositions of samples (mole fraction)			Phases observed
SnO_2	$AlO_{1.5}$	ZnO	
0.333	0.333	0.333	SnO_2, Zn_2SnO_4(ss), $ZnAl_2O_4$
1.000	0	0	SnO_2
0	1.000	0	α-Al_2O_3
0	0	1.000	ZnO
0.100	0.200	0.700	ZnO, Zn_2SnO_4(ss), $ZnAl_2O_4$
0.313	0.020	0.667	SnO_2, Zn_2SnO_4(ss)
0.667	0.020	0.313	SnO_2, Zn_2SnO_4(ss)
0	0.667	0.333	$ZnAl_2O_4$
0.333	0	0.667	Zn_2SnO_4
0.220	0.650	0.130	α-Al_2O_3, SnO_2, $ZnAl_2O_4$
0.200	0.100	0.700	ZnO, Zn_2SnO_4(ss), $ZnAl_2O_4$
0.333	0.233	0.433	SnO_2, Zn_2SnO_4(ss), $ZnAl_2O_4$
0.120	0.650	0.230	α-Al_2O_3, SnO_2, $ZnAl_2O_4$
0	0.982	0.018	ZnO, α-Al_2O_3
0.490	0.020	0.490	SnO_2, Zn_2SnO_4(ss)
0.024	0.622	0.354	Zn_2SnO_4(ss), $ZnAl_2O_4$
0.172	0.321	0.507	Zn_2SnO_4(ss), $ZnAl_2O_4$
0.953	0.030	0.015	SnO_2, $ZnAl_2O_4$
0.015	0.658	0.327	SnO_2, $ZnAl_2O_4$
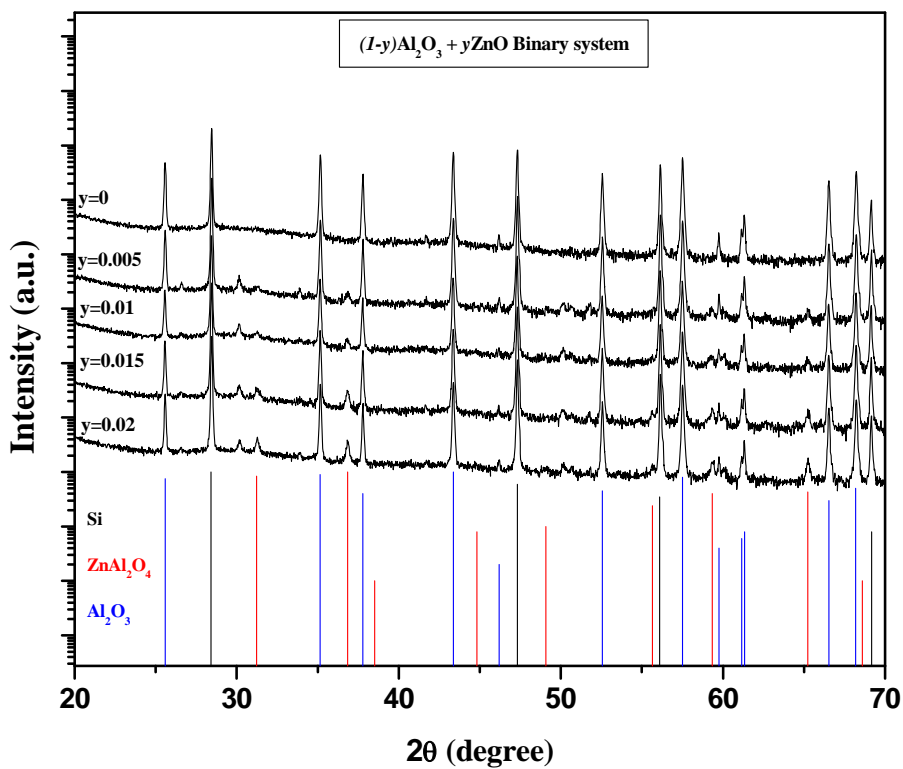
Fig. 3.3 The powder XRD patterns of the samples prepared at 1200℃ for 6 h in air. The ZnO content, y was varied from 0.005 to 0.02 mole fraction in the (1-y) Al_2O_3 + y ZnO binary system.
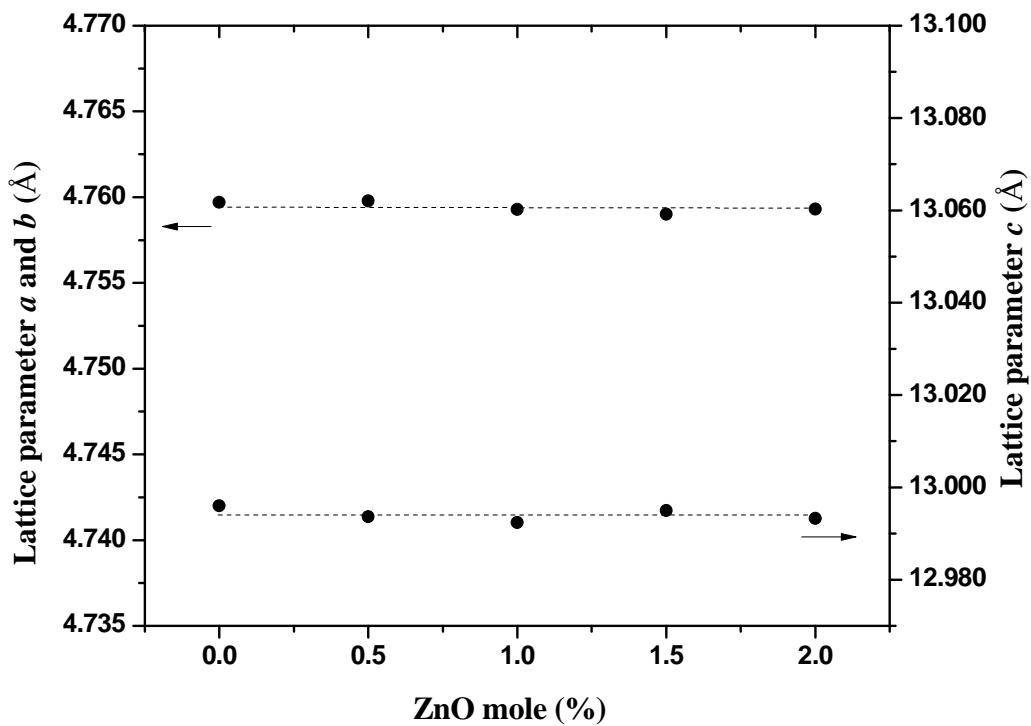
Fig. 3.4 Variation in the lattice parameter (Å) of samples as a function of ZnO mole fraction in the binary system of $(1-y)Al_2O_3 + yZnO$.
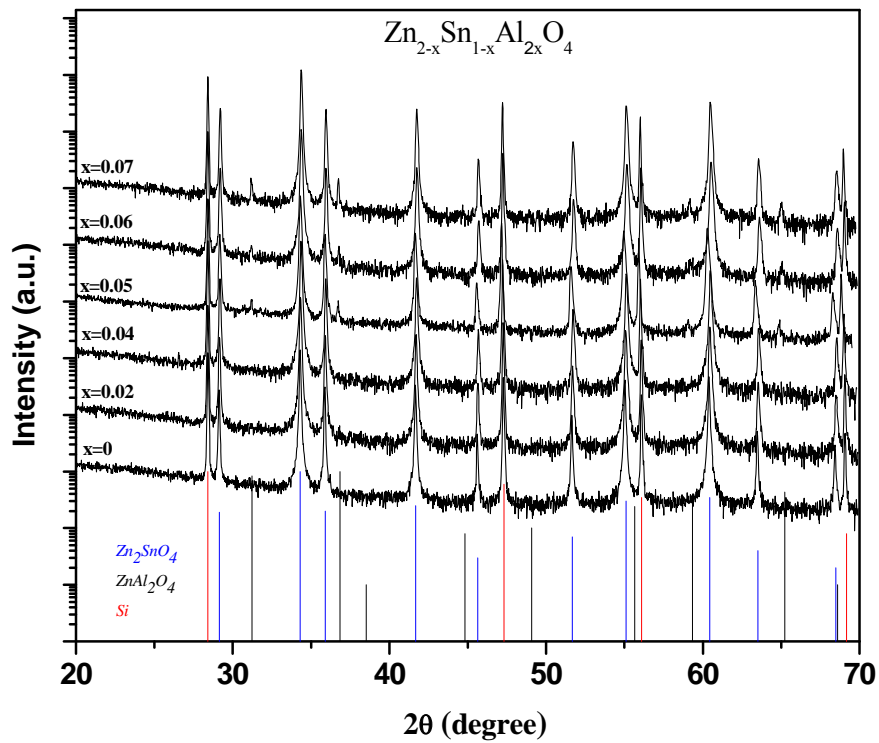
Fig. 3.5 The powder XRD patterns of the samples prepared at 1200℃ for 6 h in air. The Al content, x was varied up to 7mole % in $Zn_2Sn_{1-x}Al_xO_4$.

Table 3.2 Lattice parameters (a) of $Zn_{2-x}Sn_{1-x}Al_{2x}O_4$ ternary compounds with various Al contents, 2x.

Al content, 2x in $Zn_{2-x}Sn_{1-x}Al_{2x}O_4$ (mole fraction)	Lattice parameter a (Å)
0	8.65734(2)
0.01	8.65184(6)
0.02	8.648597(5)
0.03	8.64290(2)
0.04	8.636268(5)
0.05	8.63414(4)
0.06	8.633499(8)
0.07	8.632502(6)
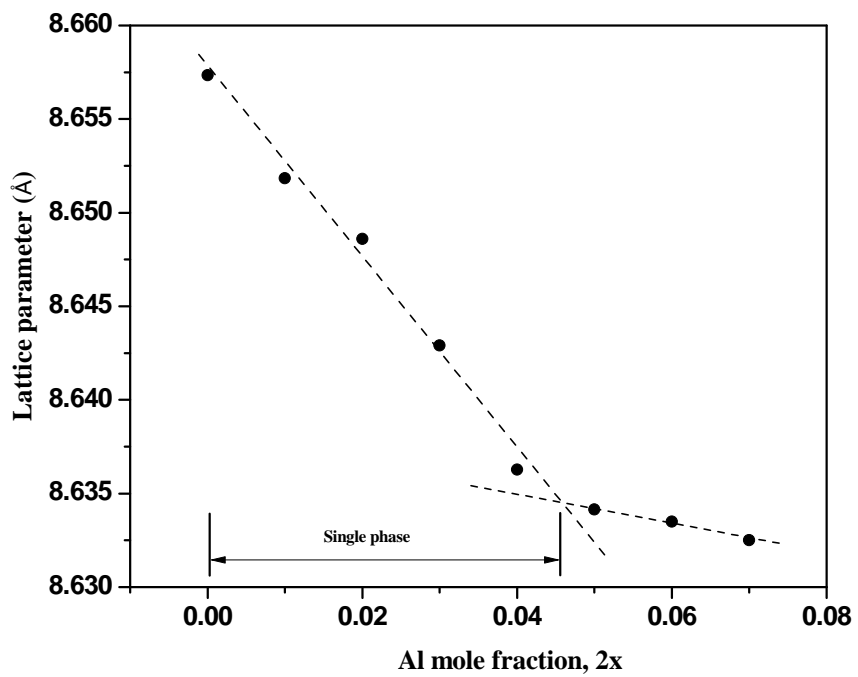
Fig. 3.6 Variation in the lattice parameters as a function of Al mole fraction, 2x in the $Zn_{2-x}Sn_{1-x}Al_{2x}O_4$ ternary compound.
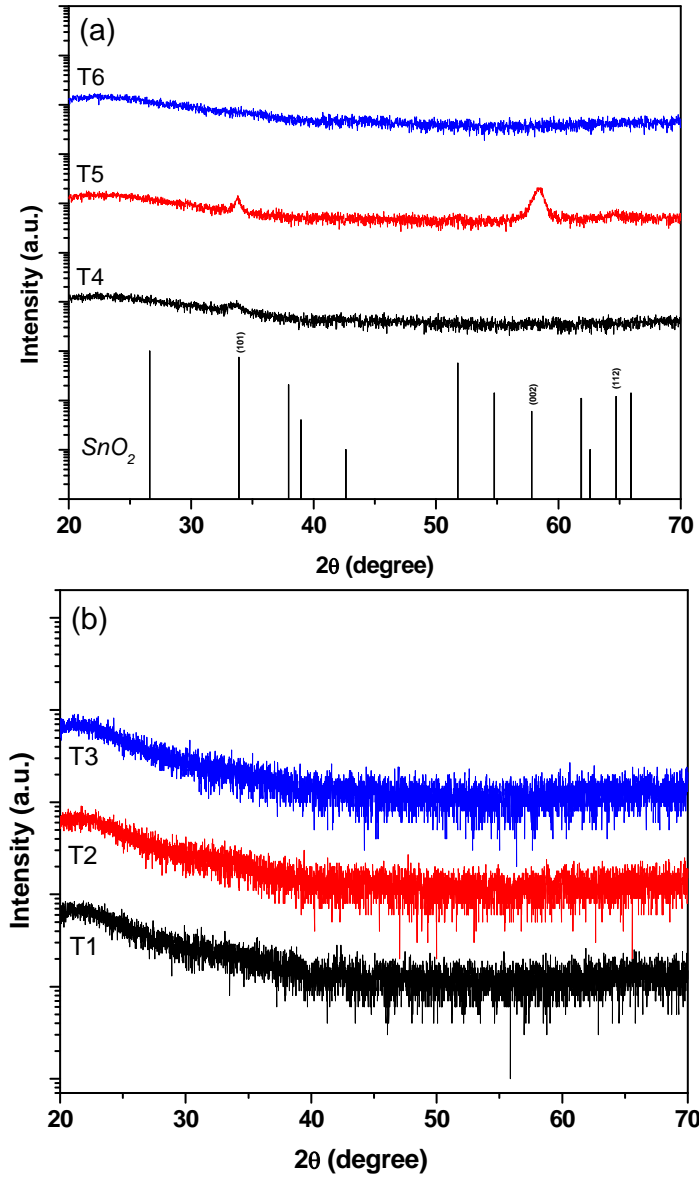
Fig. 3.7 XRD patterns of the thin films prepared using RF sputtering target of compositions (a) T4-T5, show the presence of SnO_2 crystal in the amorphous matrix and (b) T1-T3, an amorphous structure.
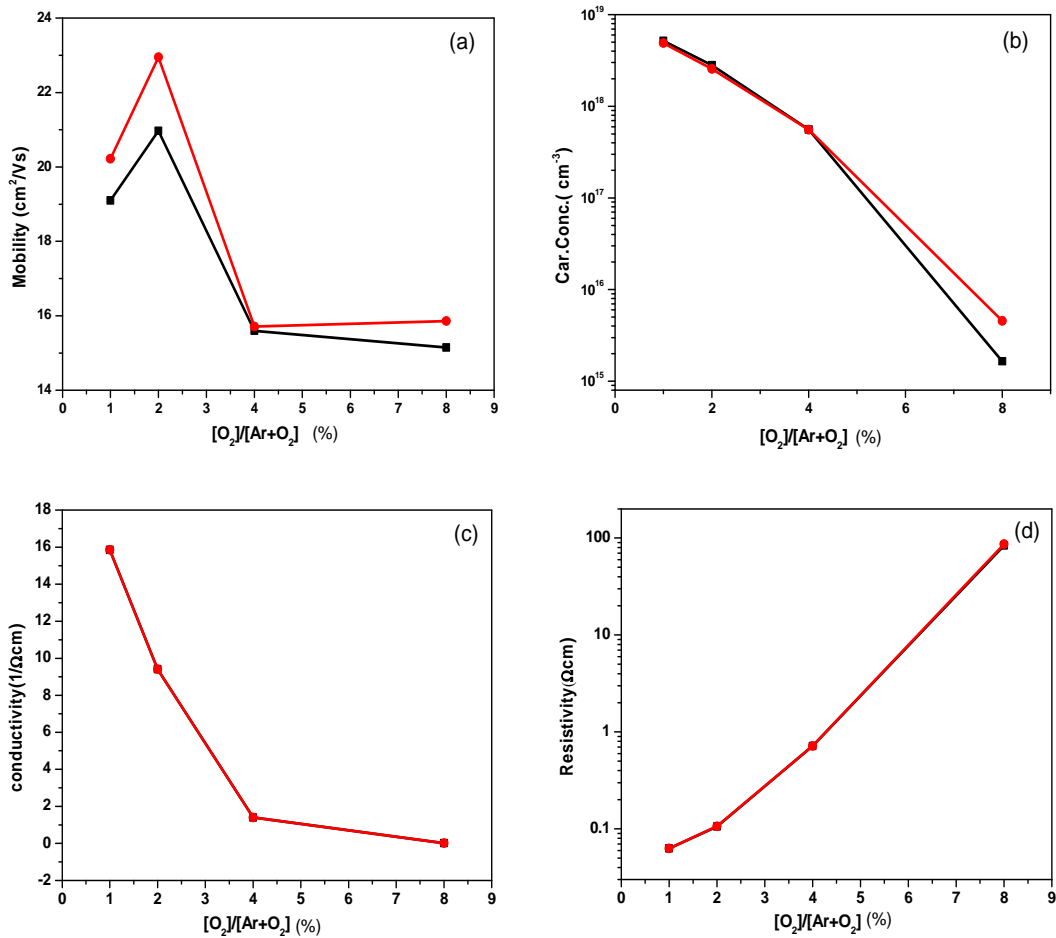
Fig. 3.8 Hall measurement data (a) mobility, (b) Carrier concentration, (c) conductivity and (d) resistivity from the thin films made with the target of composition T5 at 300ºC for different carrier gas composition (2nd set of data shows the 2nd measurement of samples).
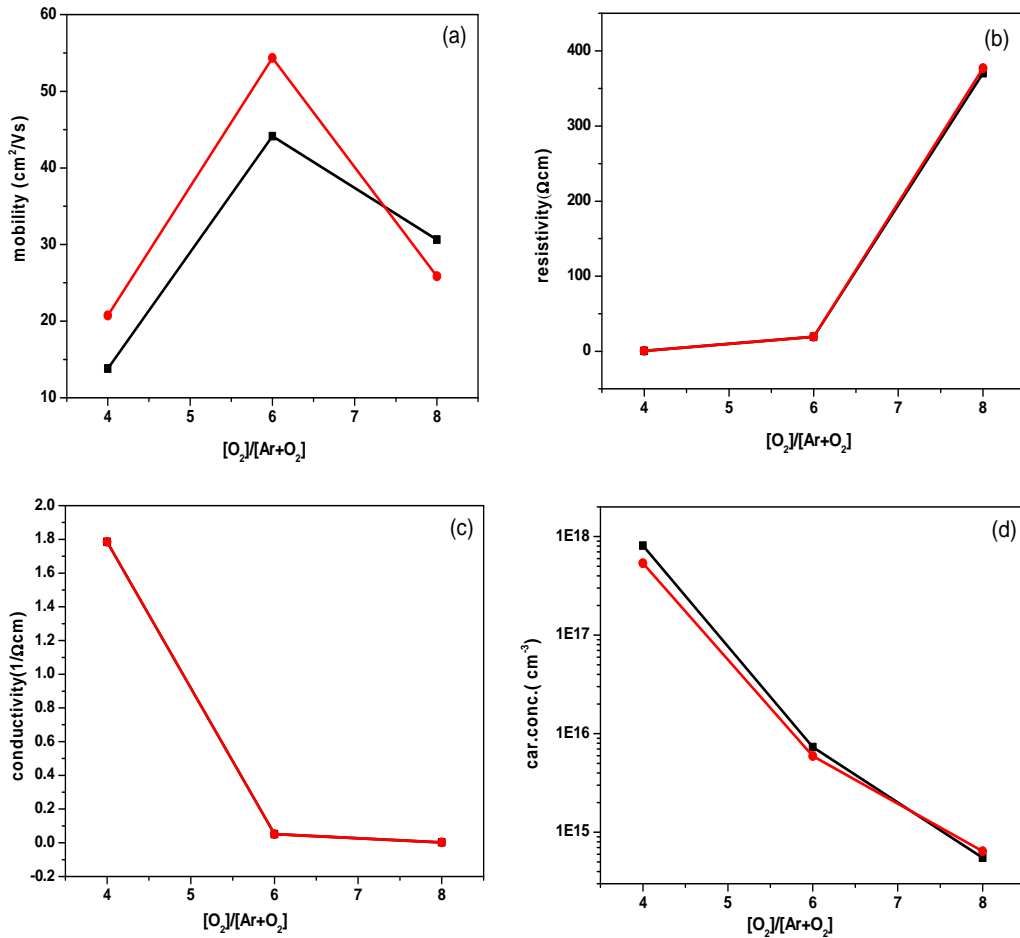
Fig. 3.9 Hall measurement data (a) mobility, (b) resistivity, (c) conductivity and (d) Carrier concentration from the thin films made with the target of composition T4 at 300ºC for different carrier gas composition (2nd set of data shows the 2nd measurement of samples).
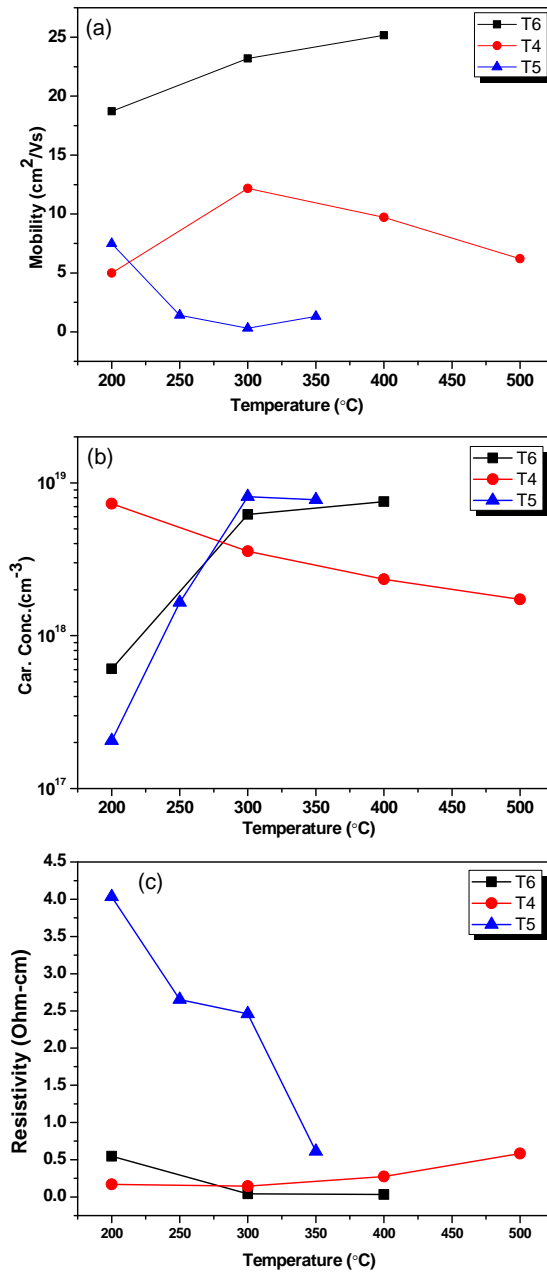
Fig. 3.10 (a) Mobility, (b) Carrier concentration and (c) Resistivity of the films prepared, using T4, T5 and T6 target at different substrate temperature.
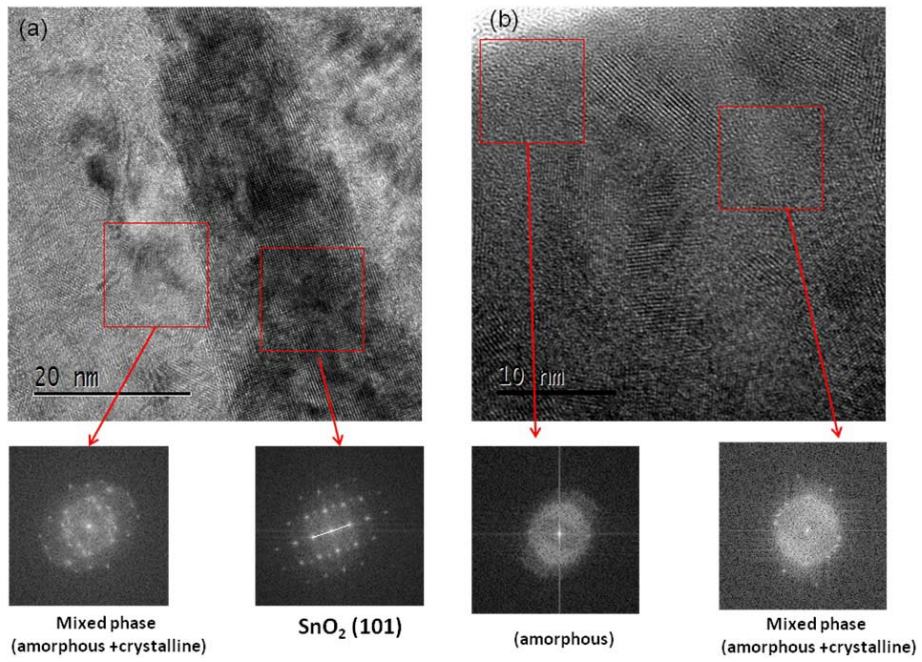
Fig. 3.11 (a and b) TEM micrographs and diffraction patterns of cross section of the film prepared using target T5.
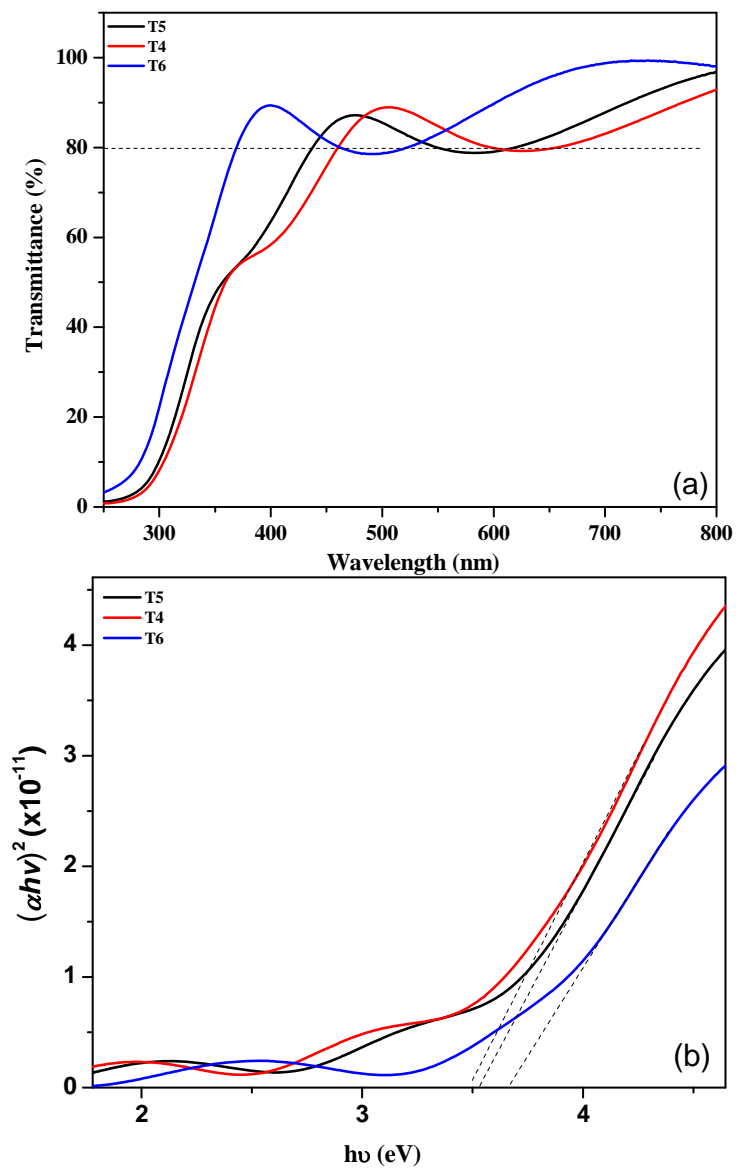
Fig. 3.12 (a) Transmittance and (b) absorbance of the thin films prepared using RF sputtering target of composition T4, T5 and T6.
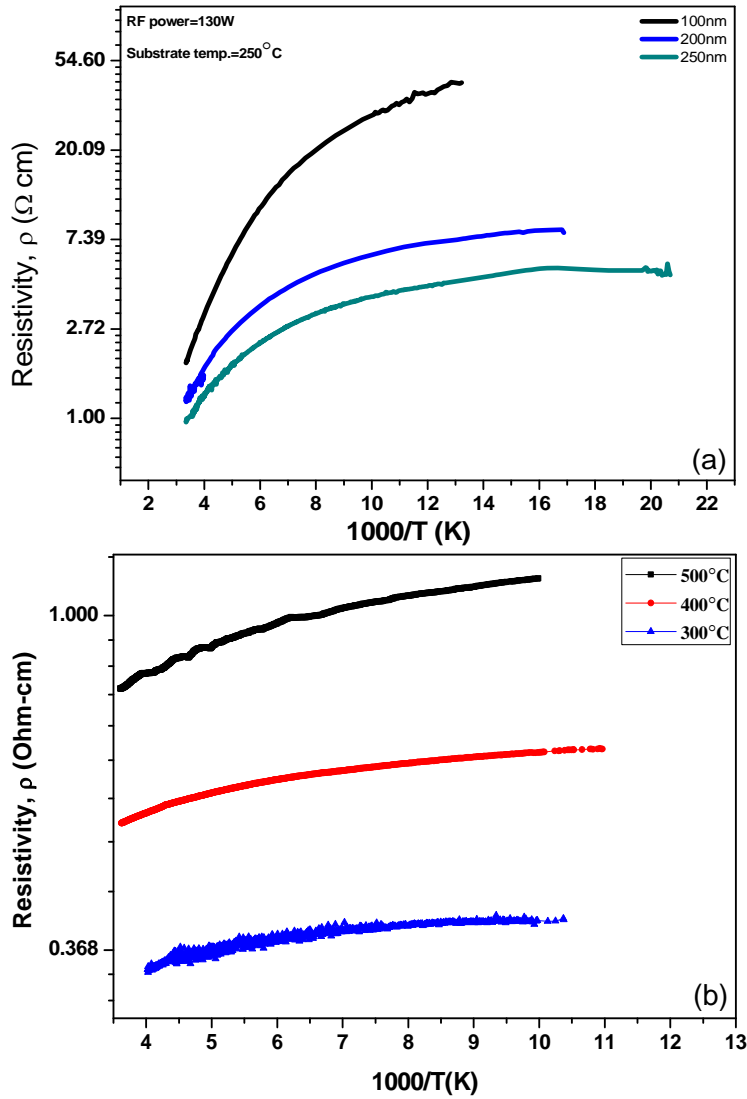
Fig. 3.13. Resistivity-Temperature (ρ-1/T) relation of the thin films prepared using RF sputtering target (a) T5, where thickness of the films vary from 100-250nm and (b) T4, where films are prepared at different temperature from 300-500ºC.
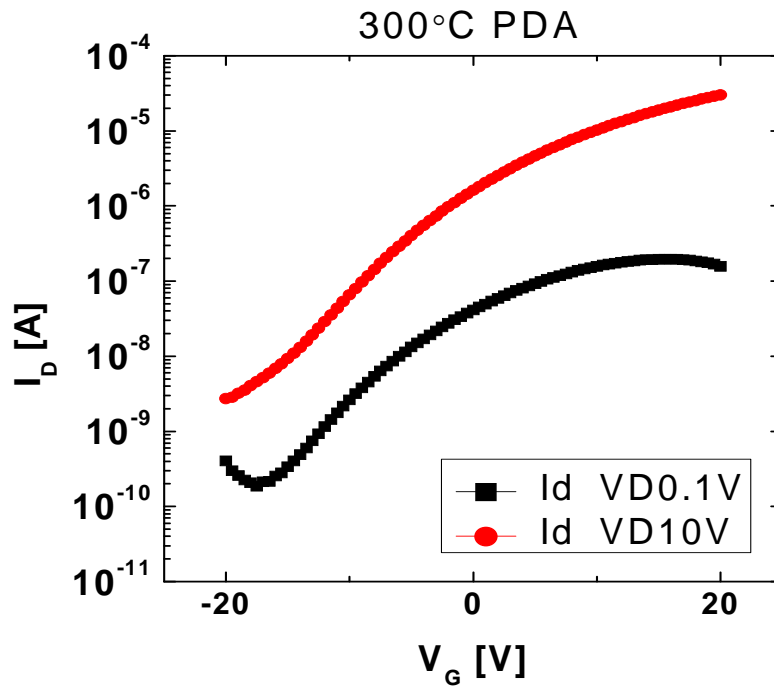
Fig. 3.14 Transfer characteristics (I$_d$-V$_g$) of the TFT device fabricated using target T5 for the active layer where I$_d$ = 0.1 and 10 volts and post deposition annealing temperature (PDA) = 300ºC.
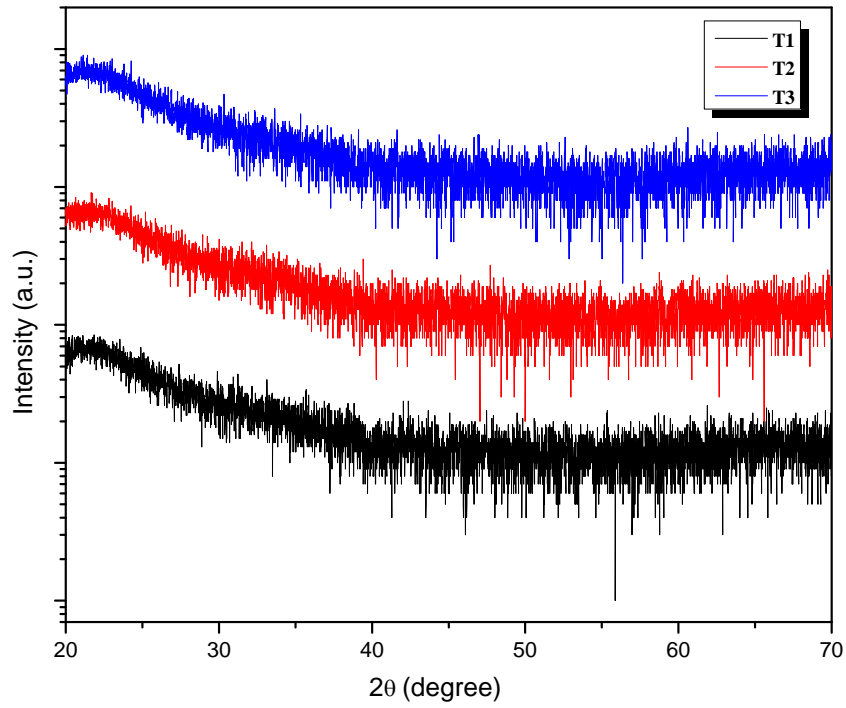
Fig. 3.15 XRD patterns of the thin films based on T1, T2 and T3 target composition.
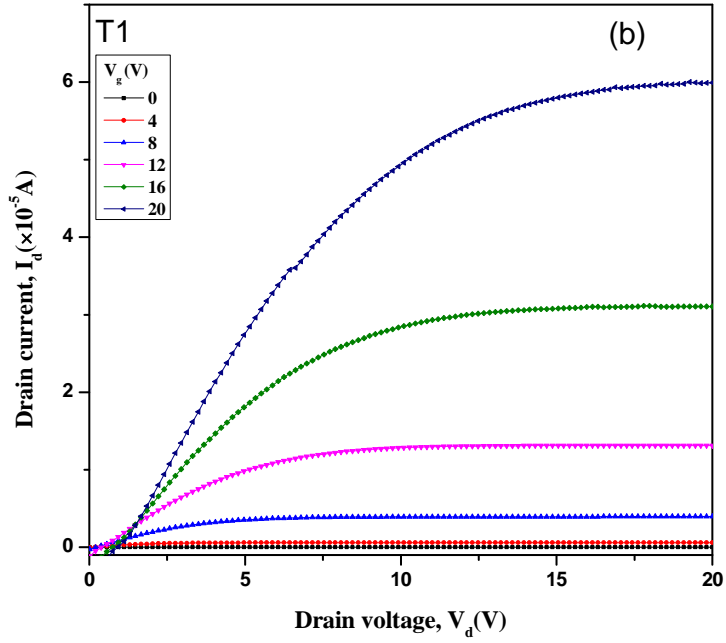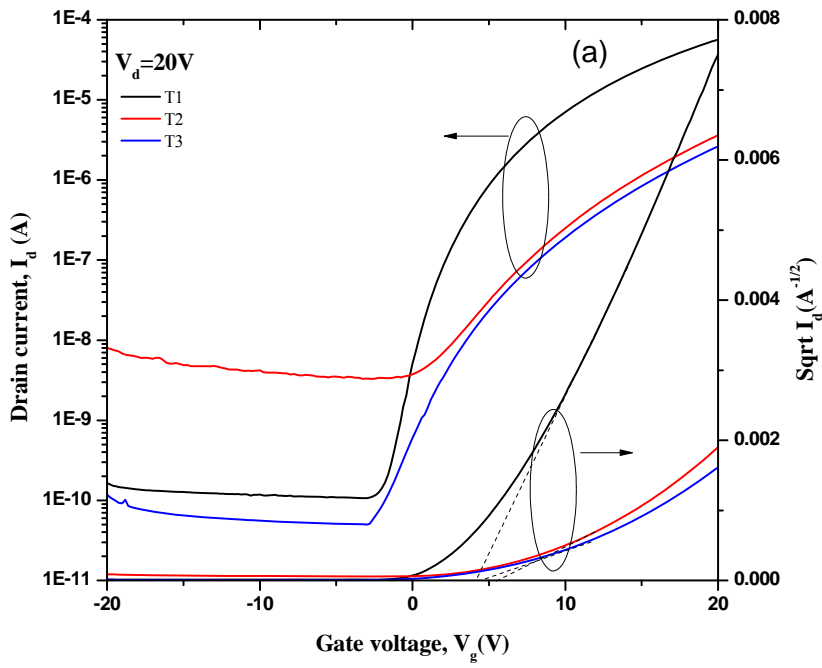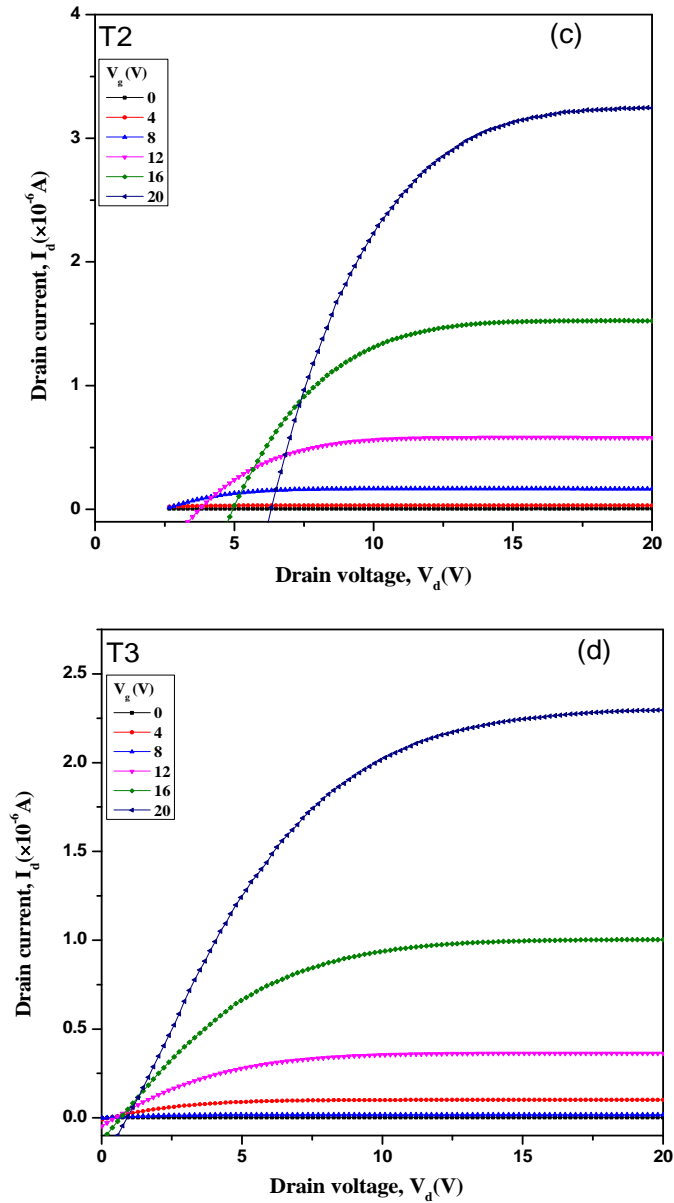
Fig. 3.16 Electrical characteristics of the T1, T2 and T3 based thin film transistor. (a) Transfer characteristics (drain current vs. gate voltage for drain voltage = 20V) and (b-d) output characteristics (drain current vs. drain voltage for various gate voltages).

Table 3.3

Device parameters including μ_{Sat}, V_{th}, SS and the *Ion/Ioff* for T1, T2 and T3 based TFTs.

Sputtering target Composition	μ_{Sat} (cm^2/Vs)	SS (V/dec)	V_{th} (V)	I_{on}/I_{off} (Ratio)
T1	5.446	1.097	3.95	5.3×10^5
T2	0.662	4.5	7.27	1.1×10^3
T3	0.461	2.23	6.38	5.2×10^4

Table 3.4

Composition of the films (T1, T2 and T3) calculated from XP spectra.

Target composition	Sn	Zn	Al	O
T1	18.31	6.25	0	75.44
T2	18.37	7.12	0	74.5
T3	18.63	6.84	3.87	70.66
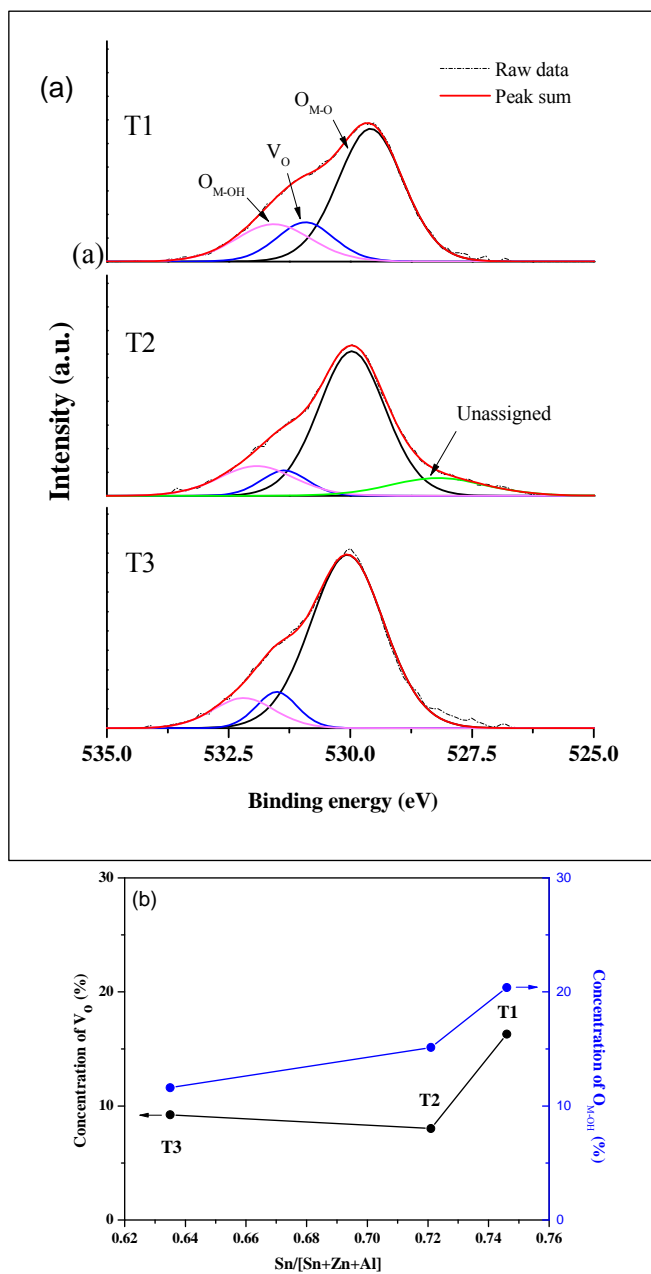
Fig. 3.17 (a)Deconvoluted O 1s XP Spectra and (b) relative fraction of O^{2-} associated with vacancies in T1, T2 and T3 films.
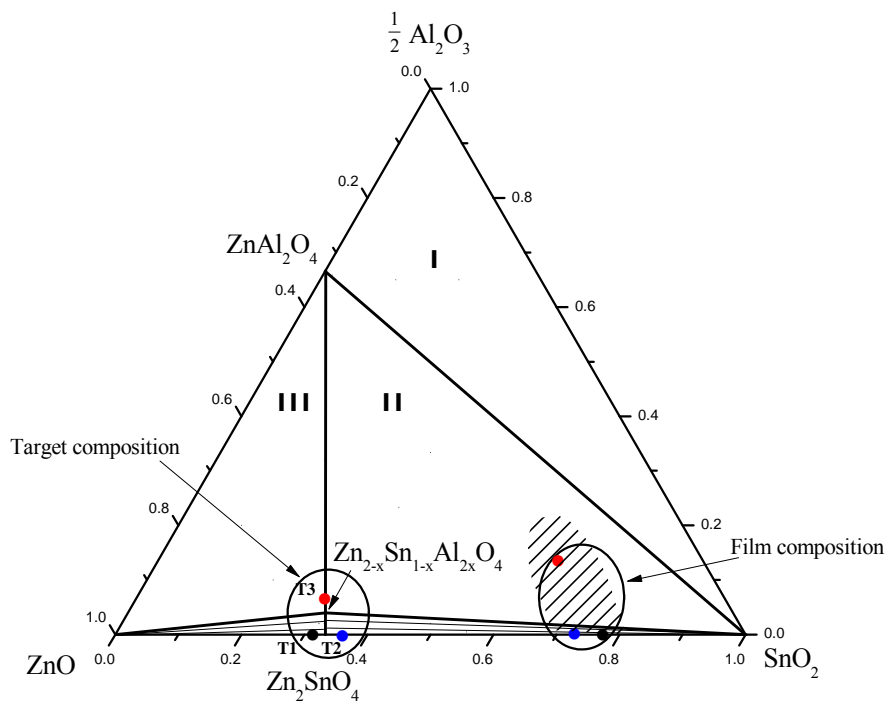
Fig. 3.18 Black, blue and red spot in the shaded region of the phase diagram represent the compositions of thin film prepared using T1, T2 and T3 target, respectively.
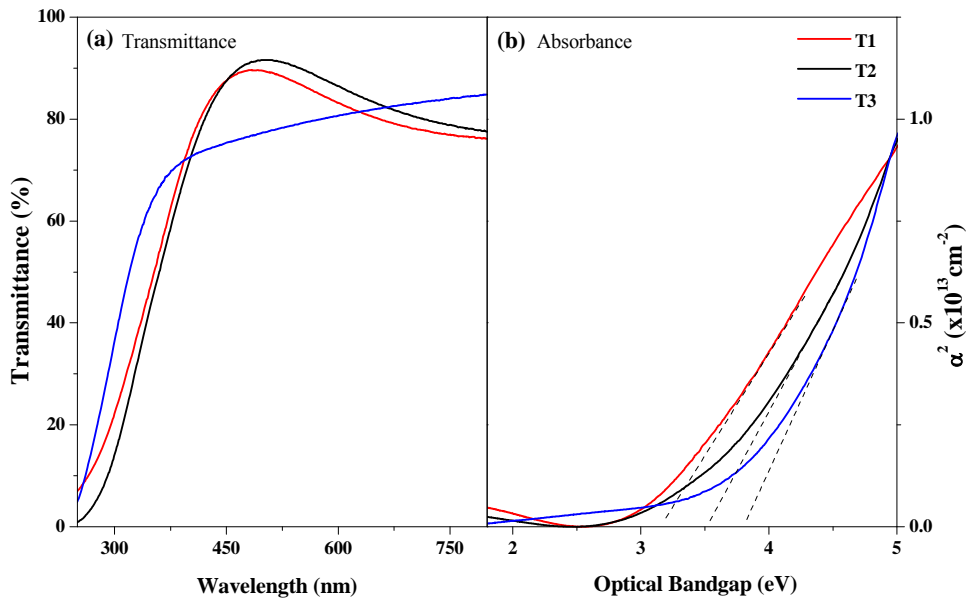
Fig. 3.19 (a) Transmittance and (b) absorbance of the thin films made from the T1, T2 and T3.

Chapter 4. Subsolidus phase relationships, structural-optical-electrical and TFT properties of the semiconducting compositions in GeO$_2$ -ZnO-SnO$_2$ ternary system

4.1 Introduction

The subsolidus phase relations in the GeO$_2$–ZnO–SnO$_2$ ternary system were investigated at 1100ºC in air. Numerous samples of various nominal compositions were prepared by the solid state reaction for this study. Two different solid solutions were found in this ternary system at 1100ºC in air. One is the ternary compounds of Zn$_2$Sn$_{1-x}$Ge$_x$O$_4$–type solid solutions and the other is the binary compounds of Sn$_{1-y}$Ge$_y$O$_2$-type solid solutions with the solubility limit of x $\approx$ 0.08 and y $\approx$ 0.06, respectively. On the other hand, although there are a few reports on Ge-doped TOSs such as ZnO[1], IGO[2], and IZO[3], GeO$_2$ has rarely been used as a dopant to TOSs. In order to find the new cost-effective indium-free TOSs, our group has focused on the Ge-doped Zn-Sn-O in the GeO$_2$–ZnO–SnO$_2$ ternary system. Unfortunately, however, although accurate information on the subsolidus phase relationships of this ternary system is invaluable to find a new TOS amorphous film, it has never been reported in the literature, which is the motivation of this study. To accurately construct the subsolidus phase diagram of the GeO$_2$–ZnO–SnO$_2$ ternary system at 1100ºC in air, we carefully investigated their subsolidus phase relationships in this work. The subsolidus phase

diagram of the GeO_2–ZnO–SnO_2 ternary system at 1100ºC in air, is represented in Fig. 4.1.

4.2 Binary systems

4.2.1 The GeO_2–SnO_2 system

Barczak *et al*.[4] reported that the melting point of SnO_2 was 1630ºC in air. However, Kohlmuller *et al*.[5] reported a complete solid solution in the form of the rutile structure for the binary GeO_2-SnO_2 system. In their phase diagram, both solidus and liquidus lines were suggested by an extrapolation of some limited experimental data, and the melting point of SnO_2 was estimated to be ~1220ºC in air. Both GeO_2 and SnO_2 crystalline phases have rutile structure in their stable state. Ionic radius of Ge^{4+} (r = 0.053nm) is smaller than that of Sn^{4+} (r = 0.069nm) [6], and thus Ge^{4+} is expected to substitute the Sn^{4+} site to form the $Sn_{1-y}Ge_yO_2$-type solid solutions. Later on, Watanabe *et al*.[7] reported that the GeO_2–SnO_2 binary system consisted of a eutectic reaction, where the melting points of h-GeO_2 and SnO_2 were 1116 and 1630°C in air, respectively. According to their report, equilibrium phases at the room temperature are t-GeO_2 and SnO_2(ss) with no intermediate compounds in this system. They also reported that while a complete solid solution between SnO_2 and GeO_2 was not formed, only around 4mol% GeO_2 was dissolved into SnO_2 at 1250°C in air, maintaining rutile structure. However, GeO_2 was transformed into hexagonal structure at 1049ºC in air. Therefore, at relatively lower temperature, it is expected to have more solubility of t-GeO_2 into t-SnO_2. In order to clarify this point, samples having the

nominal compositions of $Sn_{1-y}Ge_yO_2$, where $0 \leq y \leq 0.14$, were prepared and calcined at 1100°C in air. The XRD patterns of these samples are shown in Fig. 4.2. This figure indicates the existence of $Sn_{1-y}Ge_yO_2$-type solid solutions ($0 \leq y \leq 0.06$), where y is slightly larger than the value ($0 \leq y \leq 0.04$) at 1250 °C reported by Watanabe *et al.* [7]. Ionic radius of Ge^{4+} is ~23.2% smaller than that of Sn^{4+}, which may be major reason for this limited solid solubility. Lattice parameters as a function of Ge mole fraction, y in the $Sn_{1-y}Ge_yO_4$–type binary solid solutions are shown in Fig. 4.3. It shows a linear reduction of around 0.28 % in both *a and c* lattice parameters up to $y \approx 0.06$. GeO_2 has hexagonal structure at 1100°C in air, which seems to be another reason for its low solubility in t-SnO_2.

4.2.2 The SnO_2–ZnO system

Mihaiu *et al.*[8] reported that spinel Zn_2SnO_4 was the only stable binary compound in the SnO_2–ZnO system. The Zn_2SnO_4 (JCPDS Card No. 00-024-1470) compound possesses the inverse spinel cubic structure with the space group of Fd-3m (227), having the lattice parameter of $a =$ 8.6574 Å. All the Sn^{4+}ions occupy the octahedral sites; half of the Zn^{2+}ions go to the tetrahedral sites and another half to the octahedral sites in Zn_2SnO_4. It is also reported that the ilmenite phase of $ZnSnO_3$ prepared by an ion exchange method is stable only below 700°C in air, and it decomposes into Zn_2SnO_4 and SnO_2 at 700°C in air according to the following equation [9,10].

$$2ZnSnO_3 \rightarrow Zn_2SnO_4 + SnO_2$$
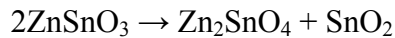
We also tried to identify the existence of ilmenite $ZnSnO_3$ in this binary system by solid state reaction but failed to obtain it at 1100ºC in air, most probably due to its thermal instability.

Mihaiu et al.[8] also reported that three phases mixture of SnO_2, ZnO and Zn_2SnO_4 was obtainable from the SnO_2–ZnO binary system at the temperature region of 900–1000ºC in air, which surely violates the Gibbs phase rule. At higher temperature regions of 1000-1500ºC, this binary system is divided into two different parts by the existence of spinel Zn_2SnO_4. One is SnO_2–Zn_2SnO_4 (0–66.6 mol% ZnO), and the other is Zn_2SnO_4–ZnO (66.6–100 mol %). According to their report, no solid solubility of ZnO in SnO_2 and SnO_2 in ZnO were found. M.K. Paria et al. [11] prepared the samples by sintering at 1250ºC in air for 4 h, and made an assumption of an interstitial solid solution up to 20% ZnO in SnO_2 on the basis of the electrical conductivity of the samples without experimental verification for the solid solubility of ZnO in SnO_2. On the other hand, Balts et al. [12] reported that a very small amount (0.7%) of ZnO was soluble into SnO_2 single crystals when the SnO_2 sample doped with 0.7% ZnO was fired at 1460ºC for 4 h in air. However, with our experimental conditions, both solid solubility of ZnO in SnO_2 and that of SnO_2 in ZnO were undetectable at 1100ºC in air.

4.2.2 The GeO_2–ZnO system

The GeO_2-ZnO binary phase diagram has never been reported yet. However, according to previous papers on the ternary systems [13,14], including both GeO_2 and ZnO endpoint phases, one spinel compound of

Zn_2GeO_4 was commonly reported as a stable equilibrium phase for this binary system. For example, according to the report by E. Takayama *et al.* [13] for the GeO_2-ZnO-Fe_2O_3 ternary system, Zn_2GeO_4 has the inverse spinel structure, and its unit cell is cubic with the space group of Fd-3m (227)(JCPDS card no. 00-025-1018) and the lattice parameter, *a* of 8.35 Å. In the inverse spinel Zn_2GeO_4, Ge^{4+} prefers to occupy the octahedral sites rather than the tetrahedral sites. Further, the $ZnGeO_3$ ilmenite structure was reported to exibit the structural phase transformation into the perovskite structure at 30.0 GPa and $1300\pm150K$[15]. However, the $ZnGeO_3$ ilmenite phase was unobtainable by the heat treatment at 1100ºC in air in this study, probably due to its thermal instability. Consequently, only spinel Zn_2GeO_4 compound was taken into consideration for this binary system.

4.3 The GeO_2–SnO_2–ZnO system

In order to construct the subsolidus phase diagram of the GeO_2–ZnO–SnO_2 ternary system at 1100ºC in air, it was necessary to know whether new ternary compounds would exist within the GeO_2–ZnO–SnO_2 system or not. For this purpose, we tried to examine the phase compatibilities between the stable solid phases experimentally reported for the binary systems.

As the first stage, to know the phase compatibility between Zn_2SnO_4 and Zn_2GeO_4 compounds, we prepared the sample with the nominal composition in the middle of the Zn_2GeO_4-Zn_2SnO_4 line (sample no. 9 in Table 1). Only two different phases of Zn_2GeO_4 and Zn_2SnO_4 were found to exist on its XRD pattern. As the second stage, we tried to

identify whether these compounds were the endpoint phases or might form a solid solution along the Zn_2GeO_4-Zn_2SnO_4 connecting line. For this purpose, samples with various nominal compositions (samples no. 6-8 in Table 1) located on the Zn_2GeO_4-Zn_2SnO_4 connecting line were prepared using the same procedure of sample preparation. Their powder XRD patterns revealed that Zn_2SnO_4 was not a linear compound but formed $Zn_2Sn_{1-x}Ge_xO_4$–type solid solutions with a solubility limit of x ≈ 0.08 while the Sn substitution for the Ge site of Zn_2GeO_4 was undetectable. The powder XRD patterns of samples with different mole fraction of GeO_2 in Zn_2SnO_4 are represented in Fig. 4.4.

We calculated the lattice parameters of samples as listed in Table 2, and also plotted them as a function of Ge composition, x in Fig. 4.5. One can see that the lattice parameters of these samples follow the Vegard's rule up to x ≈ 0.08 with an insignificant reduction (< 0.48%) in *a*. The variation in the lattice parameters of $Zn_2Sn_{1-x}Ge_xO_4$ ternary solid solutions versus x indicates that the solubility limit at 1100ºC in air is located at around 0.08 at% on the basis of the change of lattice parameter slope in Fig. 4.5. However, as shown in Fig. 4.4, the Zn_2GeO_4 second phase is undetectable for all samples over the solubility limits, i.e., from x = 0.09 to 011, on their XRD patterns. Therefore, we performed further analysis on the sample with x=0.11 to unveil this point. Fig. 4.6 represents the microstructure and EDS analysis data of this sample. The EDS mapping in Fig. 4.6(c) and spectrum in Fig. 4.6(e) show that the Ge-containing grains coexist with the $Zn_2Sn_{1-x}Ge_xO_4$ grains, obviously indicating the existence of secondary phase including Ge element above the solubility limit of x ≈ 0.08. The small Sn peaks along with large Ge and Zn peaks in the EDS spectrum corresponding to point 2 might

71

occur due to larger interaction volume of incident electrons compared with the grain size. Consequently, the solubility limit of Ge in $Zn_2Sn_{1-x}Ge_xO_4$ –type solid solutions is considered to be x ≈ 0.08 at 1100ºC in air.

These results may be primarily attributed to a large difference in ionic radii between Ge^{4+} (r = 0.053nm) and Sn^{4+} (r = 0.069nm), that is ~23.2 %, since while relatively smaller Ge^{4+} ion could partially substitute larger Sn^{4+}ion site, relatively larger Sn^{4+}ion was unable to substitute smaller Ge^{4+} ion site. In addition, metal-oxygen (M-O) bond length seems to affect the solid solubility limit of Ge in $Zn_2Sn_{1-x}Ge_xO_4$. The M-O bond lengths for Zn-O, Sn-O, and Ge-O [6,16,17] in the octahedral coordination of the spinel structure are approximately 2.09, 2.09, and 1.94Å, respectively. Compared with Zn-O and Sn-O, Ge-O has much smaller bond lengths, which can disturb the regular tetrahedral-octahedral linkage and increase the structural instability, leading to a very limited solubility (x ~ 8 mol %) of Ge in the $Zn_2Sn_{1-x}Ge_xO_4$-typesolid solutions. The solid solution line for the $Zn_2Sn_{1-x}Ge_xO_4$-type solid solutions, ranging from x = 0 to 0.08 within the $GeO_2–ZnO–SnO_2$ ternary system, divided the subsolidus phase diagram into two different phase fields composed of numerous tie lines. As shown in Fig. 4.1, one phase field is the tie lines between $SnO_2$and $Zn_2Sn_{1-x}Ge_xO_4$-type solid solutions, and the other one is the tie lines between with ZnO and$Zn_2Sn_{1-x}Ge_xO_4$-type solid solutions.

As shown in Fig. 4.1, there are three large triangular regions of I, II and III in the subsolidus phase diagram. No other new ternary phases were found for the samples having the nominal compositions within

these triangles. Instead, the following three phases were observed in these regions: GeO_2, $SnO_2(ss)$ and Zn_2GeO_4 in region I (samples no. 14-15 in Table 1), SnO_2, $Zn_2Sn_{0.92}Ge_{0.08}O_4$ and Zn_2GeO_4 in region II (samples no. 12 and 20 in Table 1), and ZnO, $Zn_2Sn_{0.92}Ge_{0.08}O_4$, and Zn_2GeO_4 phases in region III (samples no. 21 in Table 1), which correspond to the endpoint phases of each triangle.

Finally, the region surrounded by Zn_2GeO_4, $Zn_2Sn_{0.92}Ge_{0.08}O_4$, SnO_2, and GeO_2 should be divided into two sub-regions. There exited two possibilities of either the tie line between $Zn_2Sn_{0.92}Ge_{0.08}O_4$ and GeO_2 or the tie line between Zn_2GeO_4 and SnO_2. On the basis of the XRD data of the samples having the compositions on $Zn_2Sn_{0.92}Ge_{0.08}O_4$–$GeO_2$ tie line (sample no.18 in Table 1), we found that samples were composed of three different phases except those which are in the triangle between $Sn_{1-y}Ge_yO_2(ss)$ and Zn_2GeO_4, evidencing that the tie line exists between Zn_2GeO_4 and SnO_2. As previously mentioned, $Sn_{1-y}Ge_yO_2$-type solid solutions with the solubility limit of $y \approx 0.06$ was formed in the GeO_2–SnO_2 binary system, and these solid solutions coexisted with Zn_2GeO_4, and thus we could draw the tie lines between Zn_2GeO_4 and $Sn_{1-y}Ge_yO_2$-type solid solutions as shown in Fig. 4.1.

4.4 Structural, electrical, optical and TFT characteristics of Ge-doped Zn-Sn-O compositions

Fig. 4.7 shows the X-ray diffraction patterns of the various annealed thin film samples. It can be seen that the films are in amorphous state even after different oxygen concentration and annealing at 300ºC in vacuum. Films having amorphous structure are suitable for the use on flexible

substrates. In addition, absence of grain boundary (GB) helps to reduce GB traps and avoid scattering followed by increase in mobility of the charge carriers [18-20]. In addition, the FWHM of the XRD patterns are decreasing with increasing oxygen partial pressure for both the cases. This is the signature of decreasing disorder or defects with increasing oxygen concentration i.e. localized states or defects states decreases by the increasing of oxygen concentration. Fig. 4.8 shows the transmittance and absorbance of the thin film samples prepared with different $Ar:O_2$ ratio in RF sputtering. Transmittance of all the samples are ~ 80 % or above in the visible range of light, while a small increase in the optical band gap in Ge containing samples are observed. Absorbance were calculated from the transmittance data using following equation [21],

$$\alpha^2 \ = \ B\left(hv - E_{opt}\right)$$

$$\alpha = 2.303 \frac{[\log(1/T)]}{d}$$

$$hv = hc/\lambda$$

Where B is the constant, hv is the photon energy, T is the transmittance and d is the thickness of the thin films. It shows that the optical band-gap (E_{opt}) of Ge0-4 samples varied from 3.16 to 3.28eV, a wide band gap (> 3eV) which is an essential property for TAOSs. Blue shift in optical band-gap can be understood well by the Burstein-Moss (B-M) shift, which explains the dependency of band-gap widening on the increase of carrier density in the heavily doped degenerate semiconductors with high carrier density > $10^{18}cm^{-3}$ [22-25]. In case of ZTO0-4 samples, carrier

density is above 10^{18} cm^{-3} while Ge0-4 have much lower down to the range of $\sim 10^{15}$-10^{13} cm^{-3}. Although, the carrier density values are lower than 10^{18} cm^{-3}, a large shift (0.12eV) is observed in the optical band-gap for Ge0-4 samples, which seems like B-M effect. According to B-M effect, when the carrier concentration of the semiconductor increases, electrons population increases within the conduction band which pushes the Fermi level to higher energy and an increase in the optical band gap is observed (Fig. 4.13 (e)). The measured optical band-gap, $E_{opt} = E_g + \Delta E_{BM}$ is sum of intrinsic band gap (E_g) and B-M shift (ΔE_{BM}). Fig. 4.8(d) shows a large shift of 0.12eV towards higher energy in the optical band gap, from thin film sample Ge4 to Ge0, while Fig. 4.4 shows the carrier concentration of 1.02×10^{13} and 1.26×10^{16} cm^{-3} for them, respectively. However, presence of more O^{2-} ions is neutralizing more number of shallow levels, which are actually positively charged donor levels. Since the carrier density is very close to 10^{-13}-10^{-15} cm^{-3}, a very small number of free e^- are contributing to these donor level (Fig. 4.13(a-d)). Now, they are very close to the CB, an optical absorption regime (blue shaded in Fig. 4.13(d)) is being suppressed due to the neutralization of energy states (shallow defects) by increase in O^{2-} concentration. Thus, energy states (blue shaded in Fig. 4.8(d)) are forbidden for absorption. This is not B-M effect but is "like the B-M effect" (Fig. 4.13(e)).

Fig. 4.9 shows the variation of carrier density, Hall mobility and resistivity of the thin film samples as a function of O$_2$ partial pressure during sputtering. In case of ZTO0-4 samples, mobility and carrier density varies from 12.81 to 15.35 cm^2/Vs and 5.46×10^{18} to 1.72×10^{18},

respectively, while resistivity increases from 0.0892 to 0.235 Ωcm. In comparison with these, Ge0-4 samples have higher mobility from 21.76 to 17.99 cm^2/Vs, much lower carrier density from 1.26×10^{16} to 1.02×10^{13} and very high resistivity from 23.36 to 35260 Ωcm. Generally, oxide semiconductors exhibit resistivity in the range of $10-10^3 \Omega$cm [26]. A substantial increase in resistivity and decrease in carrier density with higher mobility suggests that the deep and shallow traps or defects due to oxygen vacancies (V_o) created in the films because of Sn, have been suppressed by Ge. In addition, generation of these shallow level defects may be due to Ge atoms too, as the Ge CB falls in the CB of ZnO [27,28]. Defects created by Ge are getting suppressed quickly with the increase of O^{2-} concentration which may be one of the reasons for lower carrier density in Ge0-4 films. The V_o with higher coordination number of Sn corresponds to shallow level, resulting in higher carrier density [29,30]. On the basis of our Hall measurement data we can say that the Ge4 and ZTO4 must be suitable for TFT application.

XPS spectra of O 1s core level in the thin film samples, Ge0-4 and ZTO0-4 are shown in Fig. 4.10. The O 1s spectra were deconvoluted carefully into three peaks (O $1s_{1/3}$, O $1s_{2/3}$, and O $1s_{3/3}$) to differentiate the oxygen states in the thin film samples [31]. The low binding energy peak (O $1s_{1/3}$) is related to the O^{2-} ions with metal oxides in octahedral and tetrahedral coordination, showing Ge–Zn–Sn–O bonds [32] . The O $1s_{3/3}$ peak with higher binding energy is usually contributed by chemisorbed or dissociated oxygen or OH species on the film surface, such as $-CO_3$, adsorbed H_2O, or adsorbed O_2. Third peak with

intermediate binding energy (O $1s_{2/3}$) of spectrum belongs to OH bonding species and O^{2-} ions in oxygen deficient Ge–Zn–Sn–O matrix [33]. Although, it is hard to define an oxygen vacancy (V_0) in the amorphous matrix due to the lack of order in atomic arrangement, one can consider oxygen deficient metal oxides as a site for oxygen vacancy (V_0). Q. Zhu *et al.* [34] reported the existence of Sn^{2+} ions too along with Sn^{4+} in ZTO thin films deposited at certain partial pressure of oxygen, which seems to be one of the major defect site resulting high scattering of carriers. Fig. 4.10(c) shows the relative concentration of O^{2-} ions in oxygen deficient Ge–Zn–Sn–O matrix, which is higher for the Ge containing samples. With a small increase in the O_2 partial pressure in the sputtering, the density of oxygen associated with the defects gets saturated and show no further increase even after increasing O_2 partial pressure, while ZTO samples show little fluctuation and decrease in density of O $1s_{2/3}$ peak. The density of oxygen bonding states in the defect sites increases upon doping of Ge in Zn-Sn-O, indicating a strong bonding ability of Ge atoms while poor ability of Sn with oxygen. Im *et al.* [3] reported that at lower amount of Ge doping (< 2 at%) in IZO showed an enhancement in electrical properties with increased carrier density, mobility and conductivity, while increase in the Ge concentration (>10 at%) decreased all the electrical properties of the films drastically. Lee *et al.* [35] showed a strong bonding ability of Ge with oxygen in Ge-In-Ga-O (GIGO) thin films. These reports along with our experimental data of Hall measurement and the XP spectra of O 1s shown in Fig. 4.10, confirms that Ge is a very promising candidate as a dopant in ZTO system too, which enhances the O^{2-} concentration in the oxygen deficient

Ge–Zn–Sn–O matrix and suppresses the carrier density while maintaining the mobility.

Schematic device structure for bottom gate TFT is shown in Fig. 4.11. Due to the high conductivity of the Ge0-2 and ZTO0-2, high leakage current with poor device performance was obtained; therefore, we selected Ge4 and ZTO4 for the active layer in TFT. Fig. 4.12 (a, b) represent output and transfer characteristics of the devices made with Ge4 and ZTO4 as an active layer when drain voltage V_d was set to 20V for transfer characteristics curves (drain current, I_d vs gate voltage, V_g). Data from these transfer curves were used to calculate several device parameters including saturation mobility (μ_{Sat}), threshold voltage (V_{th}), subthreshold swing *(SS) and* I_{on}/I_{off} using following equations and summarized in Table 1.

$$I_d = \frac{W}{2L}\mu_{Sat}C_i\left(V_g - V_{th}\right)^2$$

$$\mu = \frac{2L}{WC_i}\left(Slope\right)^2$$

$$SS = \frac{\partial[V_g]}{\partial[log_{10}I_d]}$$

where L is the channel length, W width and C_i the gate capacitance per unit area. In the data calculated from the transfer curve it can be noticed that the TFT of Ge4 has off current (I_{off}) approximately two orders of magnitude less, although maintaining the on current (I_{on}) of the same order of magnitude as compared to ZTO4 TFT. For the Ge4, in

comparison with ZTO4 devices, subthreshold swing, SS (V/dec) is reduced from 2.22 to 1.39V/dec, saturation mobility (μ_{sat}) slightly decreased from 6.47 to 5.29 cm^2/Vs, I$_{on}$/I$_{off}$ is increased two orders of magnitude from 4x10^4 to 2.5x10^6 and the threshold voltage (V_{th}) shifted from -4V to +5V. The charge carrier transport and current-voltage (I-V) characteristics are highly dependent on Sn and Ge content in the active layer in the devices due to their carrier and trap generation-suppression ability, respectively [36]. A positive shift in the V_{th} for the Ge containing active layer (Ge4) indicates a reduction in carrier concentration in the film which is confirmed by the Hall measurement data from Fig. 4.4. Similarly, decrease in *SS* value for this device confirms the reduction of bulk (N_{ss}) and semiconductor-gate oxide interface (D_{it}) trap densities due to Ge content. These trap density values are calculated using following equation [37].

$$SS = \frac{qk_BT(N_{ss}t_{ch} + D_{it})}{C_i log(e)}$$

where *q* is the electron charge, k_B Boltzmann constant, t_{ch} active layer thickness and *T* the absolute temperature. Values for N_{ss} and D_{it} are calculated setting one parameter zero, so that the maximum possible trap density for bulk and semiconductor-insulator interface can be obtained. Values of N_{ss} and D_{it} for both devices are summarized in Table 3. These values give clear indication of role of Ge in suppressing the traps in the ZTO4 film. Fig. 4.12(c,d) show differential conductance of output curves for the devices as a function of drain voltage and the corresponding values of total resistance, R_T and conductance, C_T between

source and drain. Contact resistance R_{S-D} is expressed in the following equations [38].

$$R_T = R_{ch} + R_{S-D} = \frac{L}{W \mu_{linear} C_i (V_g - V_{th})} + R_{S-D}$$

where R_{ch} is channel resistance, R_{S-D}, contact resistance between two electrodes and film and μ_{linear} is the mobility at the linear region of transfer curve. The R_{ch} and R_{S-D} values for Ge4 are considerably higher compared with ZTO4 active layer, which is one of the evidences that the Ge addition helped in suppressing the shallow defects level. All the values are summarized in Table 3 for comparison and Table 4 includes the relative composition of the films. Concentration of Ge in the film (~0.2 at %) was found much lower than the sputtering target composition (1.67 at %). With this small amount of Ge, device performance improved considerably. Now, it is important to note that the leakage current for the Ge4 TFT reduced approximately two orders of magnitude, SS value reduced ~0.83V/dec, I_{on} of the same order of magnitude, μ_{Sat} approximately same, V_{th} shifted to positive direction, N_{ss} reduced one order of magnitude, D_{it} reduced to half and RT reduced one order of magnitude compared to ZTO4 TFT. This considerable change in the films and device characteristics occurred with a small amount of Ge doping (< 0.2 at %).

4.5 Summery

The subsolidus phase diagram of the GeO_2–ZnO–SnO_2 ternary system at 1100ºC in air could be constructed by carefully investigating their

equilibrium solid phase relationships with powder XRD analyses of numerous samples. In addition to previously reported $Sn_{1-y}Ge_yO_2$-type binary solid solutions, new $Zn_2Sn_{1-x}Ge_xO_4$-type ternary solid solutions were found to exist, and their solubility limits are x ≈ 0.08 and y ≈ 0.06, respectively. The existence of $Zn_2Sn_{1-x}Ge_xO_4$-type solid solutions is considered to extend the potential candidate for finding a new TOS amorphous film to the GeO_2-ZnO-SnO_2 system.

The structural, optical and electrical properties of the RF sputtered thin films of ZTO and Ge-doped ZTO were examined and compared. Ge doping in ZTO doesn't alter the crystallanity and maintains amorphousity of the films along with ~80 % transmittance and large optical band-gap, E_{opt} 3.16-3.28 eV. A slight increase of O_2 partial pressure in RF sputtering reduces carrier concentration and increases resistivity considerably with a consistent high Hall mobility (~ 20 cm^2/V s) in Ge-doped films. Small amount of Ge (< 0.2 at %) doping reduced the trap density one order of magnitude in the films, which showed a strong oxygen binding ability of Ge. Introduction of Ge in the ZTO films improved the transport properties of the TFT devices exhibiting mobility, SS, V_{th}, and I_{on}/I_{off} of 5.29 cm^2/Vs, 1.39 V/decade, +5 V and 2.5 x10^6, respectively. Although, the performance reported for the TFT devices are superior to this, its ease of fabrication and cost effectiveness make Ge-doped Zn-Sn-O an attractive and promising material for the further study.

References

1   Arita, M., Yamaguchi, M. & Masuda, M. Electrical and optical properties of germanium-doped zinc oxide thin films. *Materials transactions* **45**, 3180-3183 (2004).

2   Nag, A. & Shireen, A. Search for new transparent conductors: Effect of Ge doping on the conductivity of , and. *Solid State Communications* **150**, 1679-1682, doi:10.1016/j.ssc.2010.06.025 (2010).

3   Im, Y. J. *et al.* Improvement in the Electrical Performance of Ge-Doped InZnO Thin-Film Transistor. *Journal of Nanoscience and Nanotechnology* **15**, 7537-7541, doi:10.1166/jnn.2015.11156 (2015).

4   Barczak, V. & Insley, R. Phase Equilibria in the System Al2O3—SnO2. *Journal of the American Ceramic Society* **45**, 144-144 (1962).

5   Kohlmuller, J. F. a. R. PbO-SnO and GeO_2-SnO_2 Systems. *Bull. Soc. Chim. Fr.* **12**, 4283-4286 (1970).

6   Shannon, R. t. Revised effective ionic radii and systematic studies of interatomic distances in halides and chalcogenides. *Acta Crystallographica section A: crystal physics, diffraction, theoretical and general crystallography* **32**, 751-767 (1976).

7   Watanabe, A., Kikuchi, T., Tsutsumi, M., Takenouchi, S. & Uchida, K. Solid Solubility of GeO2 in SnO2. *Journal of the American Ceramic Society* **66** (1983).

8   Mihaiu, S. *et al.* Advanced ceramics in the SnO2–ZnO binary
        system. *Ceramics International* **41**, 4936-4945,
        doi:10.1016/j.ceramint.2014.12.056 (2015).

9   Al-Hinai, M. H., Al-Hinai, A. T. & Dutta, J. Phase
        transformation behavior of zinc metastannates obtained by
        aqueous precipitation at different temperatures. *Journal of
        Materials Science* **49**, 7282-7289 (2014).

10   Gou, H. *et al.* Energetic stability, structural transition, and
        thermodynamic properties of ZnSnO[sub 3]. *Applied Physics
        Letters* **98**, 091914, doi:10.1063/1.3562013 (2011).

11   Paria, M. K. & Maiti, H. S. Electrical conductivity of
        polycrystalline tin dioxide and its solid solution with ZnO.
        Journal of Materials Science **18**, 2101-2107,
        doi:10.1007/bf00555004 (1983).

12   Balts, K. W.   (eds E. E. Kohnke & Joel J. Martin) (Oklahoma
        State University, 1970).

13   Takayama, E. The system GeO 2 瑕 ZnO 瑕 Fe 2 O 3 at 1000° C.
        Journal of Solid State Chemistry **44**, 426-428 (1982).

14   Brown, J. J. & Hummel, F. Reactions between ZnO and selected
        oxides of elements of groups IV and V. *BRIT CERAM SOC
        TRANS* **64**, 419-435 (1965).

15   Yusa, H. *et al.* High-pressure transformations of ilmenite to
        perovskite, and lithium niobate to perovskite in zinc germanate.
        Physics and Chemistry of Minerals **33**, 217-226,
        doi:10.1007/s00269-006-0070-5 (2006).

16   Wei, S.-H. & Zhang, S. First-principles study of cation distribution in eighteen closed-shell A II B 2 III O 4 and A IV B 2 II O 4 spinel oxides. *Physical Review B* **63**, 045112 (2001).

17   Garbato, A., Garbato, L., Marrocu, P. & Sedda, F. Solid Solubility in Mixed Spinels ZnMIII2O4-Zn2SnO4 (MIII= Al, Ga). *Japanese Journal of Applied Physics* **39**, 134 (2000).

18   Ellmer, K. & Mientus, R. Carrier transport in polycrystalline transparent conductive oxides: A comparative study of zinc oxide and indium oxide. *Thin Solid Films* **516**, 4620-4627, doi:10.1016/j.tsf.2007.05.084 (2008).

19   Pei, Z. *et al.* Optical and electrical properties of direct-current magnetron sputtered ZnO: Al films. *Journal of Applied Physics* **90**, 3432-3436 (2001).

20   Ellmer, K. Resistivity of polycrystalline zinc oxide films: current status and physical limit. *Journal of Physics D: Applied Physics* **34**, 3097 (2001).

21   Lee, Y.-S., Chen, W.-J., Huang, J.-S. & Wu, S.-C. Effects of composition on optical and electrical properties of amorphous In–Ga–Zn–O films deposited using radio-frequency sputtering with varying O2 gas flows. *Thin Solid Films* **520**, 6942-6946, doi:10.1016/j.tsf.2012.07.106 (2012).

22   Saw, K. G., Aznan, N. M., Yam, F. K., Ng, S. S. & Pung, S. Y. New Insights on the Burstein-Moss Shift and Band Gap Narrowing in Indium-Doped Zinc Oxide Thin Films. *PLOS ONE* **10**, e0141180, doi:10.1371/journal.pone.0141180 (2015).

23   Burstein, E. Anomalous optical absorption limit in InSb. *Physical Review* **93**, 632 (1954).

24   Kamat, P. V., Dimitrijevic, N. M. & Nozik, A. Dynamic Burstein-Moss shift in semiconductor colloids. *The Journal of Physical Chemistry* **93**, 2873-2875 (1989).

25   Sarkar, A., Ghosh, S., Chaudhuri, S. & Pal, A. K. Studies on electron transport properties and the Burstein-Moss shift in indium-doped ZnO films. *Thin Solid Films* **204**, 255-264, doi:http://dx.doi.org/10.1016/0040-6090(91)90067-8 (1991).

26   Iwasaki, T. *et al.* Combinatorial approach to thin-film transistors using multicomponent semiconductor channels: An application to amorphous oxide semiconductors in In–Ga–Zn–O system. *Applied Physics Letters* **90**, 242114, doi:10.1063/1.2749177 (2007).

27   Lin, L., Xiong, K. & Robertson, J. Atomic structure, electronic structure, and band offsets at Ge:GeO:GeO[sub 2] interfaces. *Applied Physics Letters* **97**, 242902, doi:10.1063/1.3525371 (2010).

28   Sevik, C. & Bulutay, C. Theoretical study of the insulating oxides and nitrides: SiO2, GeO2, Al2O3, Si3N4, and Ge3N4. *Journal of Materials Science* **42**, 6555-6565, doi:10.1007/s10853-007-1526-9 (2007).

29   Kamiya, T., Nomura, K. & Hosono, H. Present status of amorphous In-Ga-Zn-O thin-film transistors. *Sci Technol Adv Mater* **11**, 044305, doi:10.1088/1468-6996/11/4/044305 (2010).

30   Ágoston, P., Albe, K., Nieminen, R. M. & Puska, M. J. Intrinsic n-Type Behavior in Transparent Conducting Oxides: A Comparative Hybrid-Functional Study of ${\mathrm{In}}_{2}{\mathbf{O}}_{3}$, ${\mathrm{SnO}}_{2}$, and ZnO. *Physical Review Letters* **103**, 245501 (2009).

31   Byung Du, A., Jun Hyung, L., Mann-Ho, C., Jin-Seong, P. & Kwun-Bum, C. Thin-film transistor behaviour and the associated physical origin of water-annealed In–Ga–Zn oxide semiconductor. *Journal of Physics D: Applied Physics* **45**, 415307 (2012).

32   Chen, M., Pei, Z. L., Sun, C., Wen, L. S. & Wang, X. Surface characterization of transparent conductive oxide Al-doped ZnO films. *Journal of Crystal Growth* **220**, 254-262, doi:http://dx.doi.org/10.1016/S0022-0248(00)00834-4 (2000).

33   Ok, K.-C. *et al.* Semiconducting behavior of niobium-doped titanium oxide in the amorphous state. *Applied Physics Letters* **100**, doi:10.1063/1.3698389 (2012).

34   Zhu, Q. *et al.* Structural and physical properties of transparent conducting, amorphous Zn-doped SnO2 films. *Journal of Applied Physics* **115**, 033512, doi:10.1063/1.4861378 (2014).

35   Lee, K.-H., Ok, K.-C., Kim, H. & Park, J.-S. The influence of oxygen partial pressure on the performance and stability of Ge-doped InGaO thin film transistors. *Ceramics International* **40**, 3215-3220 (2014).

36   Kim, Y. J. *et al.* Impact of the cation composition on the electrical performance of solution-processed zinc tin oxide thin-

film transistors. *ACS Appl Mater Interfaces* **6**, 14026-14036, doi:10.1021/am503351e (2014).

37   Greve, D. W. *Field effect devices and applications: devices for portable, low-power, and imaging systems*. (Prentice-Hall, Inc., 1998).

38   Kim, H. *et al.* The effects of the surface morphology of poly(3,4-ethylenedioxythiophene) electrodes on the growth of pentacene, and the electrical performance of the bottom contact pentacene transistor. *Solid-State Electronics* **67**, 70-73, doi:https://doi.org/10.1016/j.sse.2011.08.001 (2012).

Table 4.1. Samples with various nominal compositions in the GeO_2-ZnO -SnO_2 ternary system and their equilibrium phases analyzed by powder XRD.

| Sample no.	Nominal compositions of samples (mole fraction)			Phases observed
	SnO_2	GeO_2	ZnO	
1	0.033	0.300	0.667	Zn_2GeO_4, Zn_2SnO_4
2	0.017	0.317	0.667	Zn_2GeO_4, Zn_2SnO_4
3	0.007	0.327	0.667	Zn_2GeO_4, Zn_2SnO_4
4	0.333	0	0.667	Zn_2SnO_4
5	0	0.333	0.667	Zn_2GeO4
6	0.300	0.033	0.667	Zn_2GeO_4,Zn_2SnO_4
7	0.317	0.017	0.667	$Zn_2Sn_{1-x}Ge_xO_4$ (ss)
8	0.327	0.007	0.667	$Zn_2Sn_{1-x}Ge_xO_4$ (ss)
9	0.167	0.167	0.667	Zn_2GeO_4, Zn_2SnO_4
10	0.971	0.010	0.020	Zn_2GeO_4, SnO_2
11	0.864	0.045	0.091	Zn_2GeO_4, SnO_2
12	0.036	0.321	0.643	Zn_2GeO_4, SnO_2, $Zn_2Sn_{1-x}Ge_xO_4$ (ss)
13	0.017	0.328	0.655	Zn_2GeO_4, SnO_2
14	0.010	0.971	0.020	Zn_2GeO_4, $Sn_{1-y}Ge_yO_2$ (ss), $GeO2$
15	0.045	0.864	0.091	Zn_2GeO_4, $Sn_{1-y}Ge_yO_2$ (ss), GeO_2
16	0.321	0.036	0.643	Zn_2SnO_4, SnO_2
17	0.328	0.017	0.655	Zn_2SnO_4, SnO_2
18	0.250	0.250	0.500	Zn_2GeO_4, $Sn_{1-y}Ge_yO_2$ (ss)
19	0.525	0.475	0.100	Zn_2GeO_4, SnO_2, GeO_2
20	0.474	0.060	0.465	Zn_2GeO_4, SnO_2, $Zn_2Sn_{1-x}Ge_xO_4$ (ss)
21	0.097	0.095	0.807	Zn_2GeO_4, ZnO, $Zn_2Sn_{1-x}Ge_xO_4$ (ss)
22	0.475	0.525	0.100	Zn_2GeO_4, Zn_2SnO_4
23	0.267	0.067	0.667	Zn_2GeO_4, Zn_2SnO_4
24	0.233	0.100	0.667	Zn_2GeO_4, Zn_2SnO_4
25	0.216	0.116	0.667	Zn_2GeO_4, Zn_2SnO_4
26	0.200	0.133	0.667	Zn_2SnO_4, SnO_2
27	0.980	0.020	0	$Sn_{1-y}Ge_yO_2$ (ss)
28	0.960	0.040	0	$Sn_{1-y}Ge_yO_2$ (ss)
29	0.940	0.060	0	$Sn_{1-y}Ge_yO_2$ (ss), GeO_2
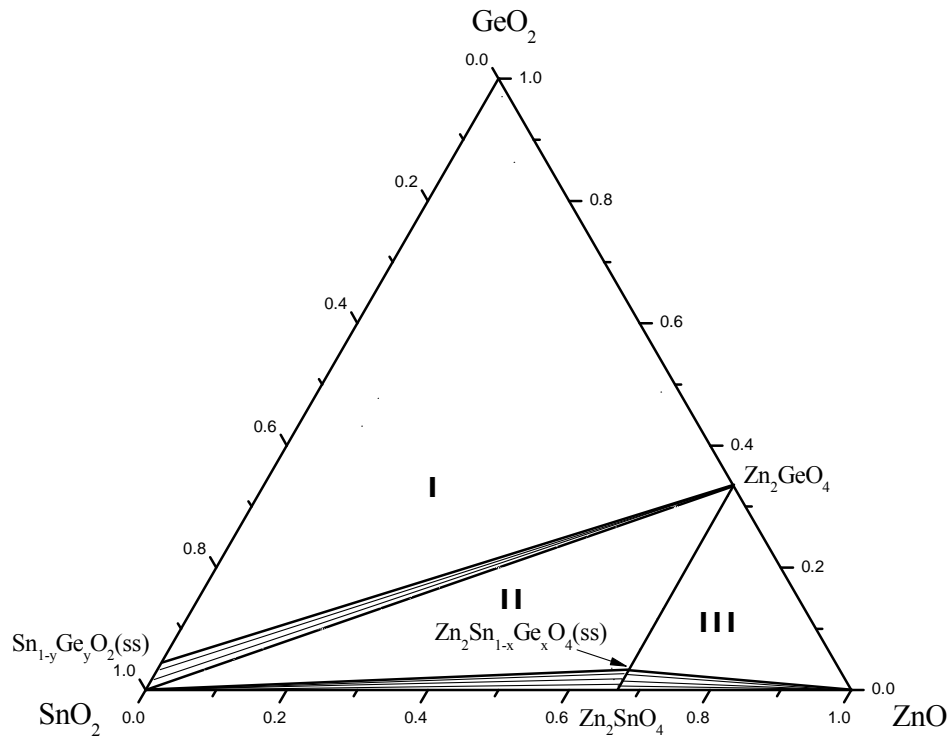
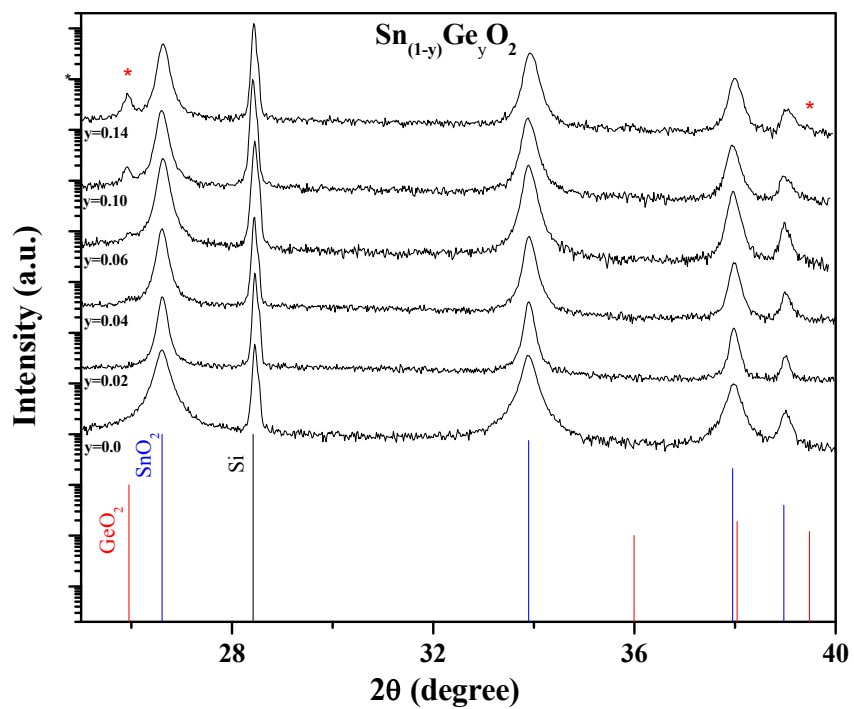Fig..4.1. The subsolidus phase diagram for the GeO_2–SnO_2–ZnO ternary system at 1100°C in air.

Fig. 4.2. The powder XRD patterns of the samples prepared at 1100℃ for 6 h in air. The Ge content, y was varied up to 14 mol% in $Sn_{1-y}Ge_yO_2$.
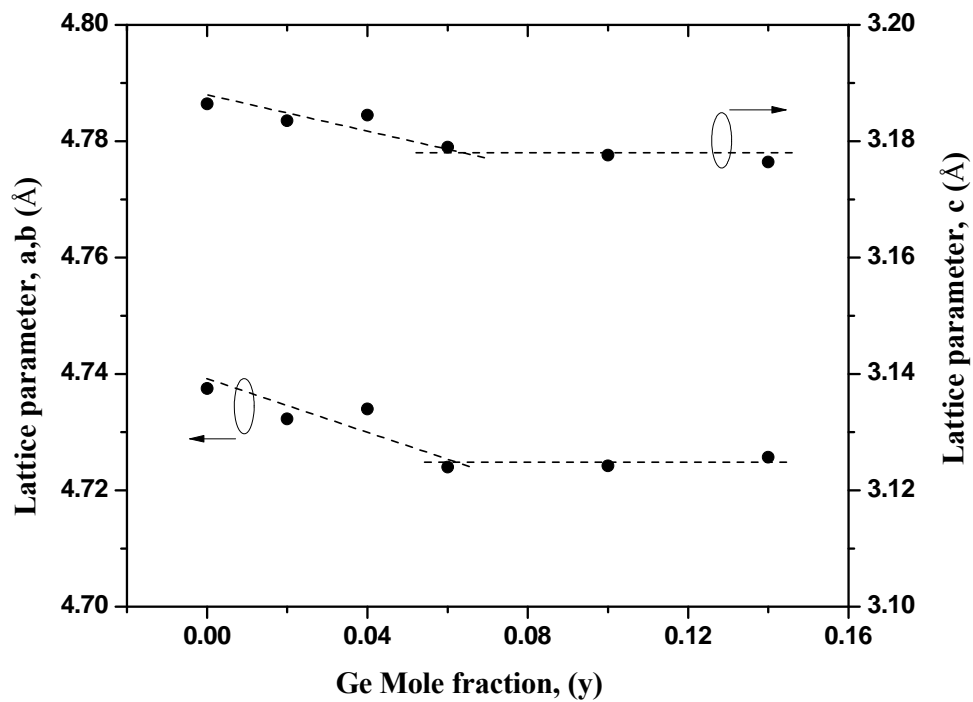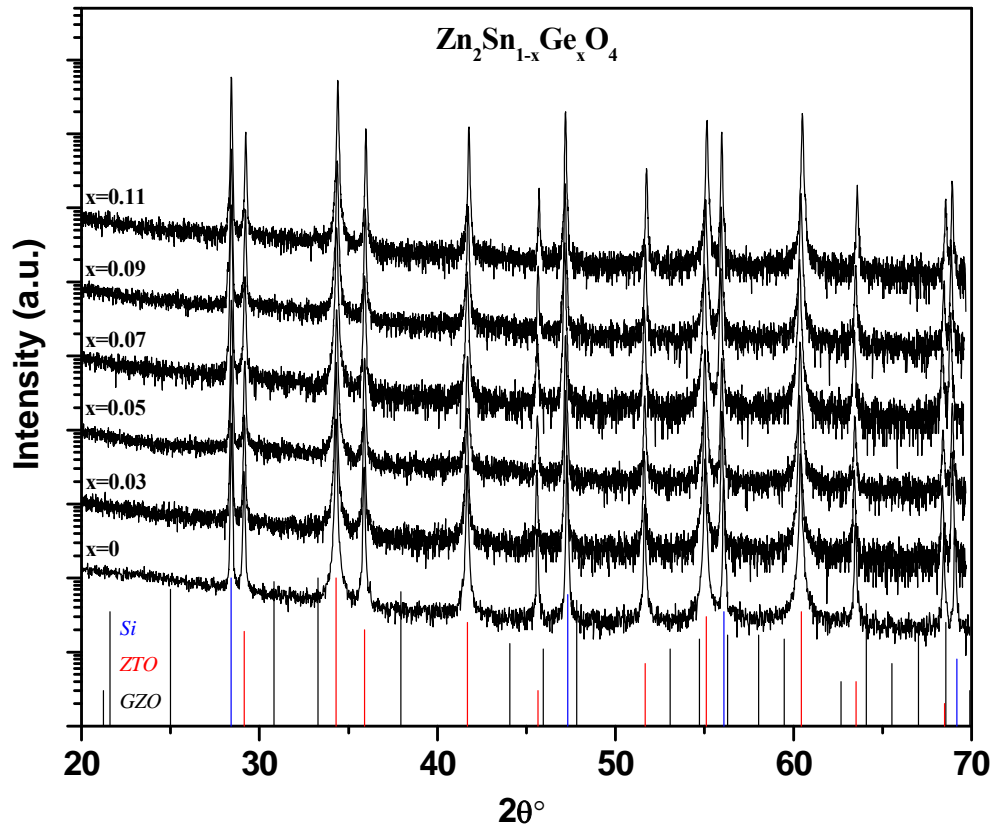
Fig. 4.3. The lattice parameters of tetragonal $Sn_{1-y}Ge_yO_4$ binary compounds as a function of Ge mole fraction, y.

Fig. 4.4. The powder XRD patterns of the samples prepared at 1100℃ for 6 h in air. The Ge content, x was varied up to 11mol% in $Zn_2Sn_{1-x}Ge_xO_4$.

Table 4.2. Lattice parameters of cubic $Zn_2Sn_{1-x}Ge_xO_4$ ternary compounds with various Ge content, x.

Ge content, x in $Zn_2Sn_{1-x}Ge_xO_4$ (mole fraction)	Lattice parameter, a (Å)
0.00	8.65734(2)
0.01	8.6469(3)
0.03	8.63578(2)
0.05	8.6275(4)
0.06	8.621(1)
0.07	8.61608(4)
0.08	8.61345(5)
0.09	8.61276(3)
0.11	8.61135(2)
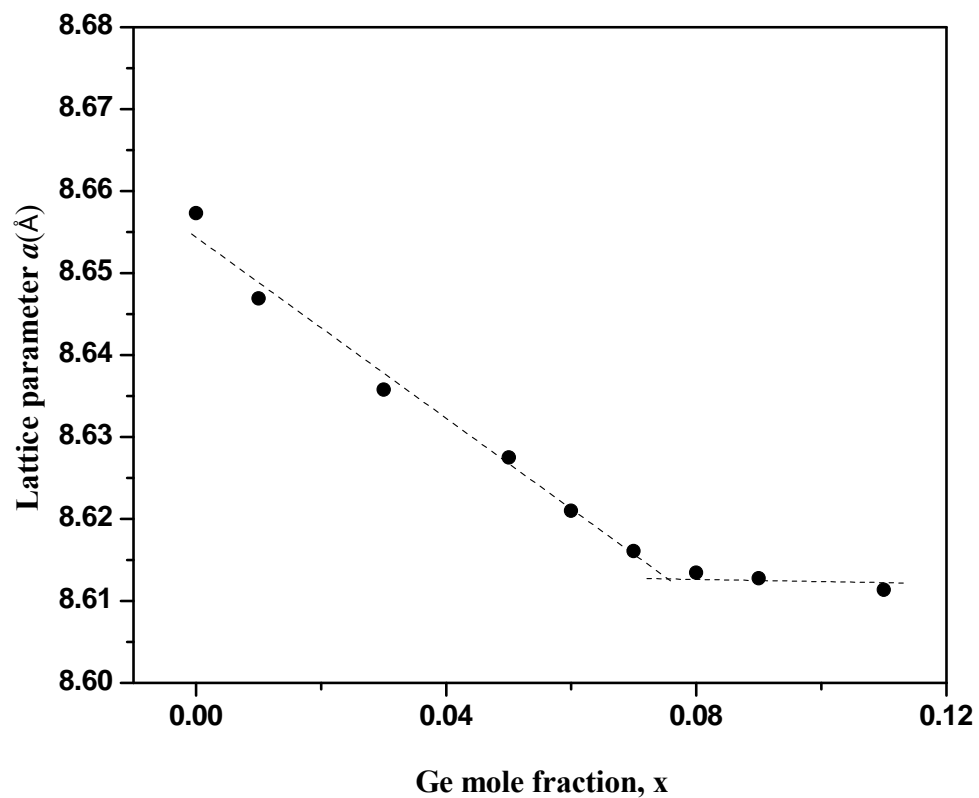
Fig. 4.5. Lattice parameters of cubic $Zn_2Sn_{1-x}Ge_xO_4$ ternary compounds as a function of Ge mole fraction, x.
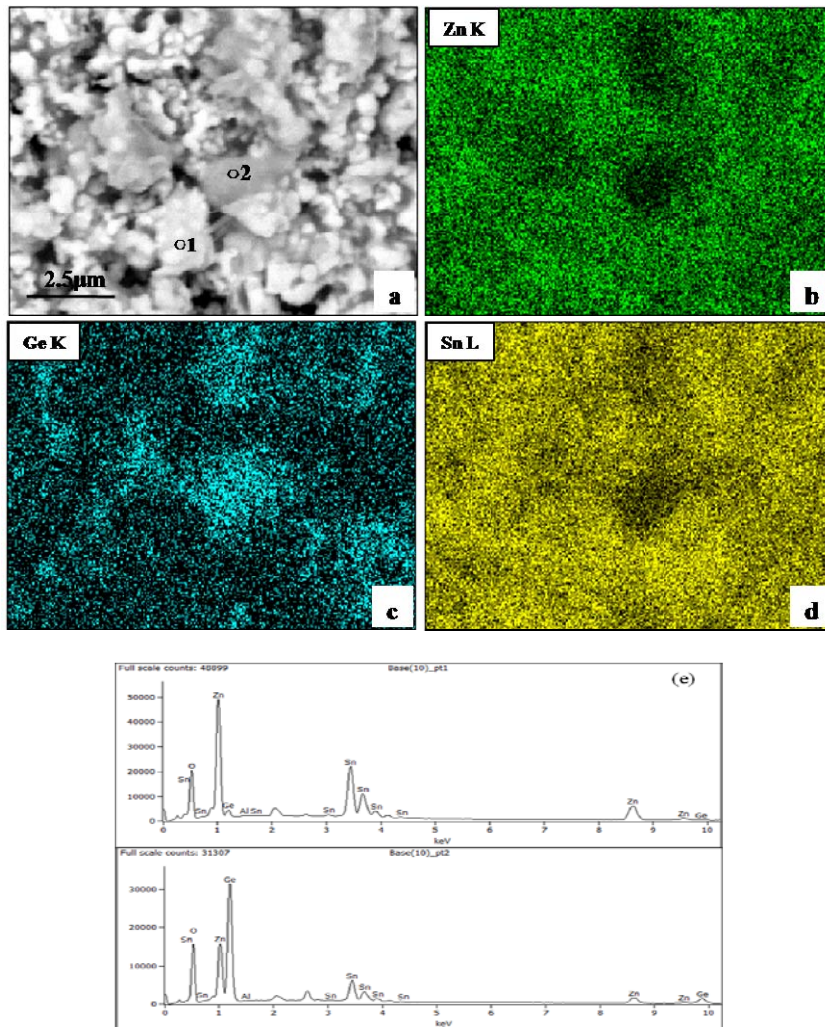
Fig. 4.6 (a) Back scattered electrons (BSE) micrograph, (b, c and d) EDS mapping of Zn, Ge and Sn, respectively, and (e) EDS analysis spectra obtained from the points 1 and 2 in (a) for the sample with x = 0.11. Top and bottom spectra in (e) are from the points 1 and 2, respectively.
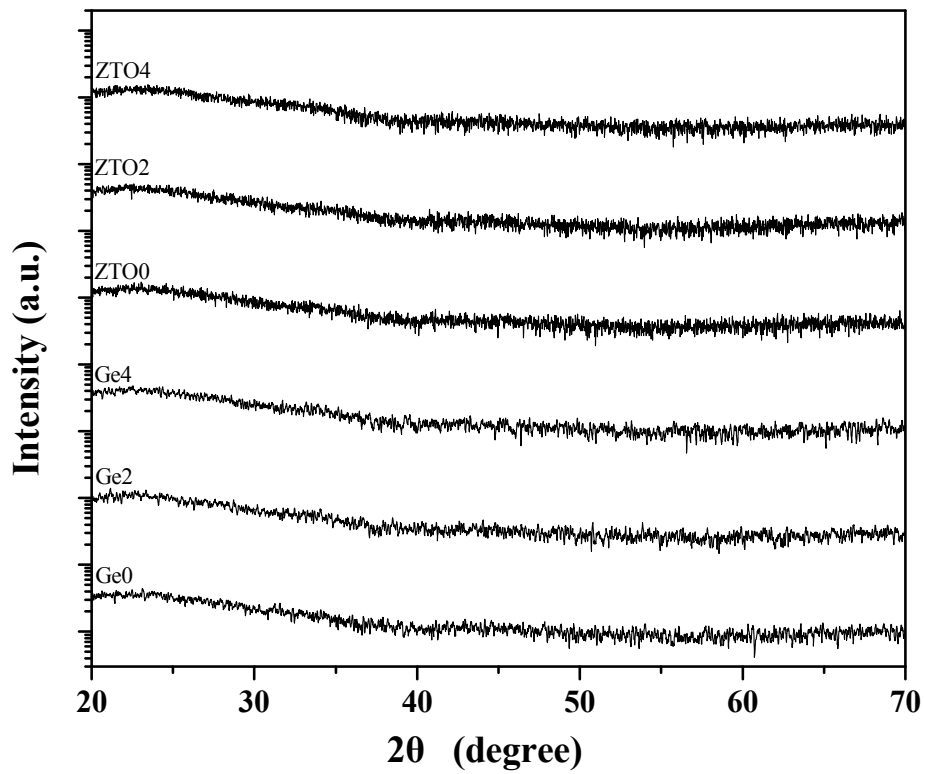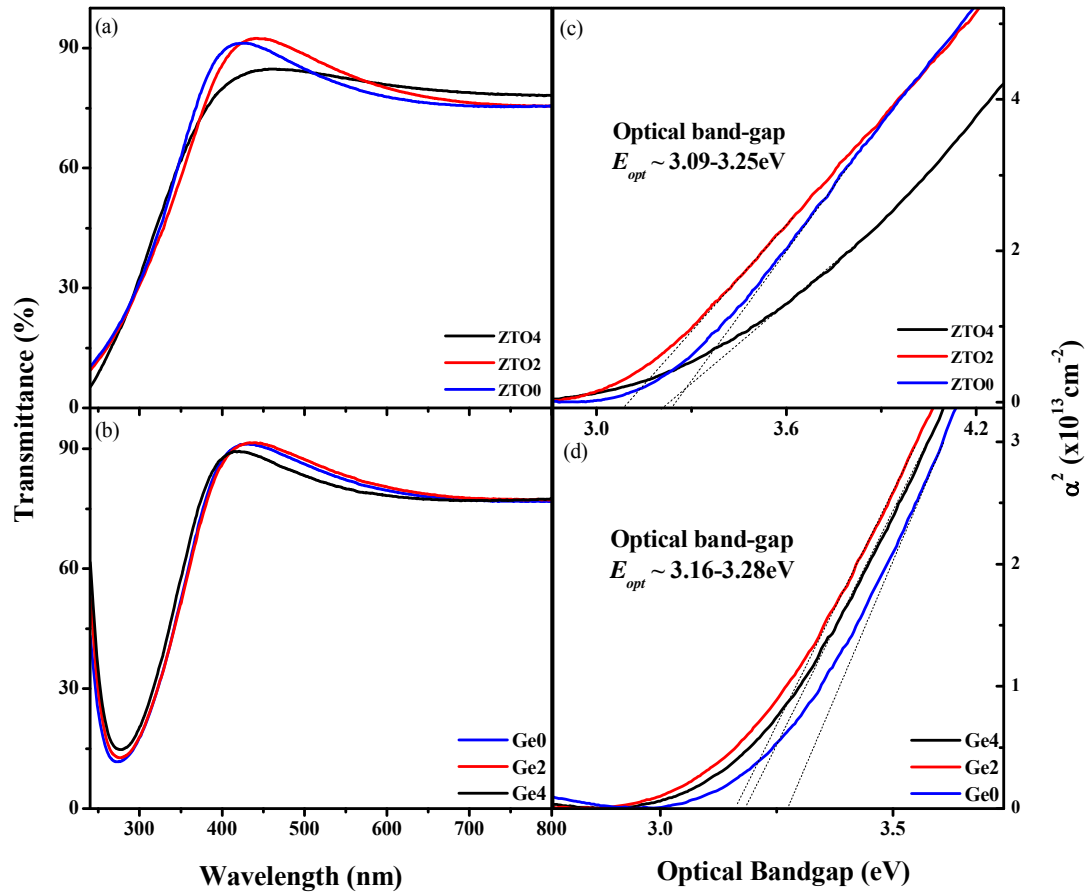
Fig. 4.7 XRD patterns of the thin films Ge0-4 and ZTO0-4.

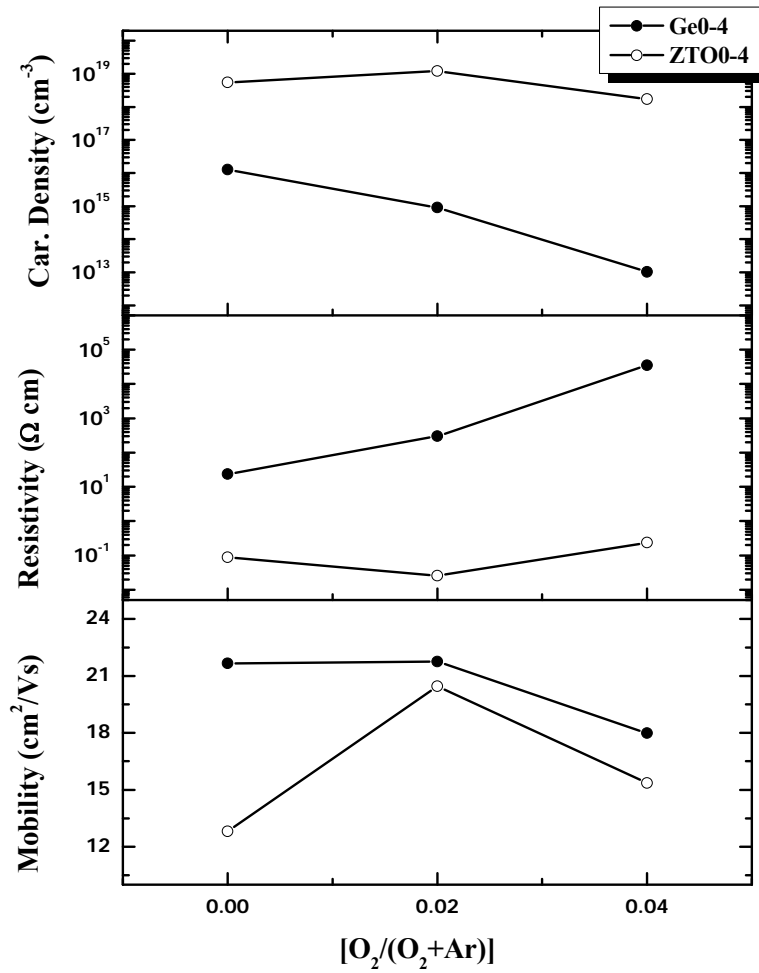Fig. 4.8 (a,b) Transmittance with their corresponding (c,d) absorbance for the thin films of Ge0-4 and ZTO0-4.

Fig. 4.9 Carrier density, resistivity and mobility for the thin film samples of Ge0-Ge4 and ZTO0-ZTO4, obtained from the Hall measurement.
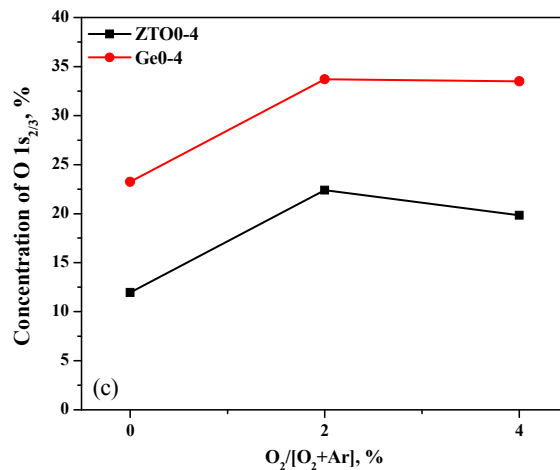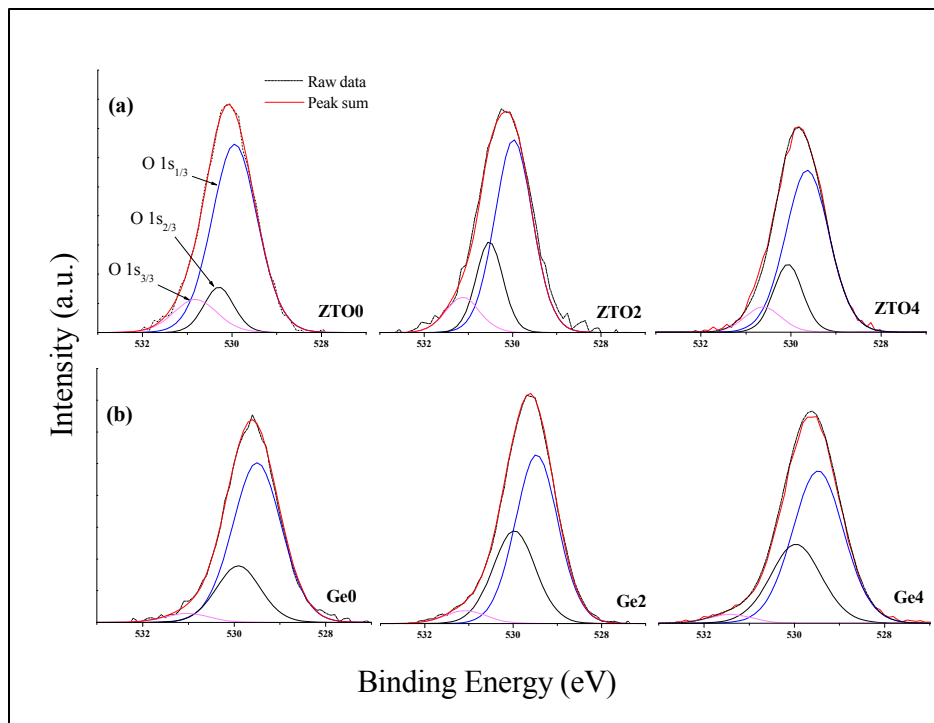
Fig.4.10 XP spectra of O 1s core level and their deconvolution results for the (a) Ge0-4, (b) ZTO0-4 and (c) relative concentration of O^{2-} ions in oxygen deficient Ge–Zn–Sn–O matrix in the thin films.
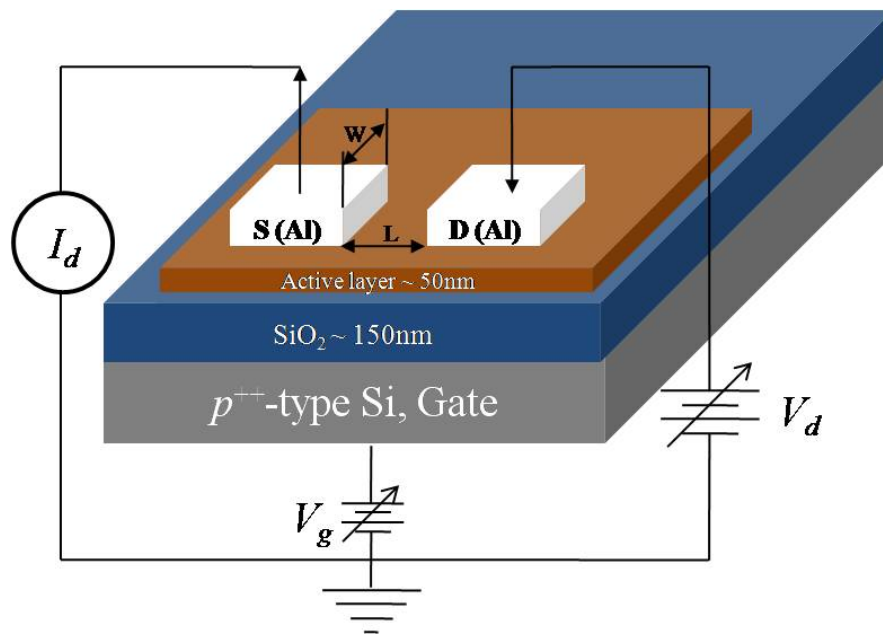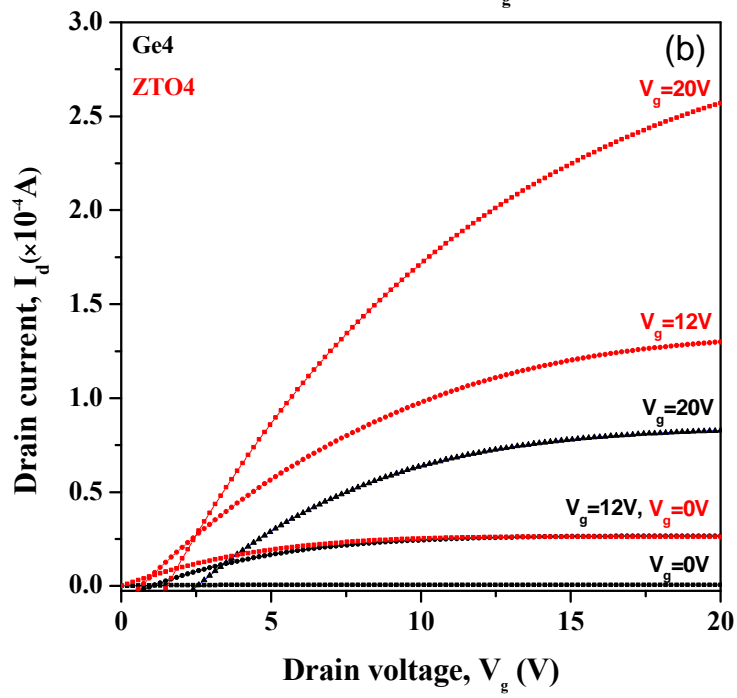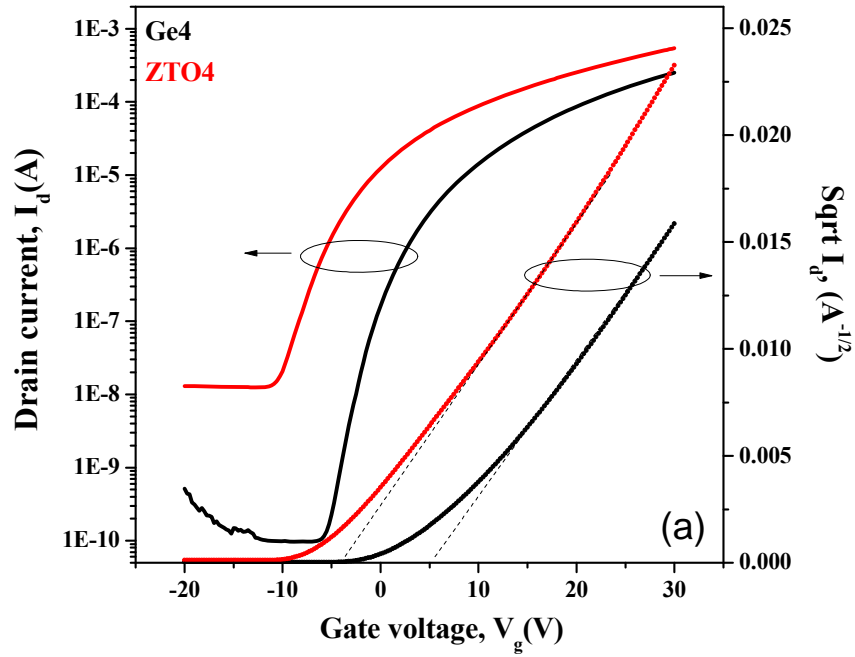
Fig. 4.11 Schematic diagram of bottom-gate TFT device structure where active layers are thin films of Ge4 or ZTO4.
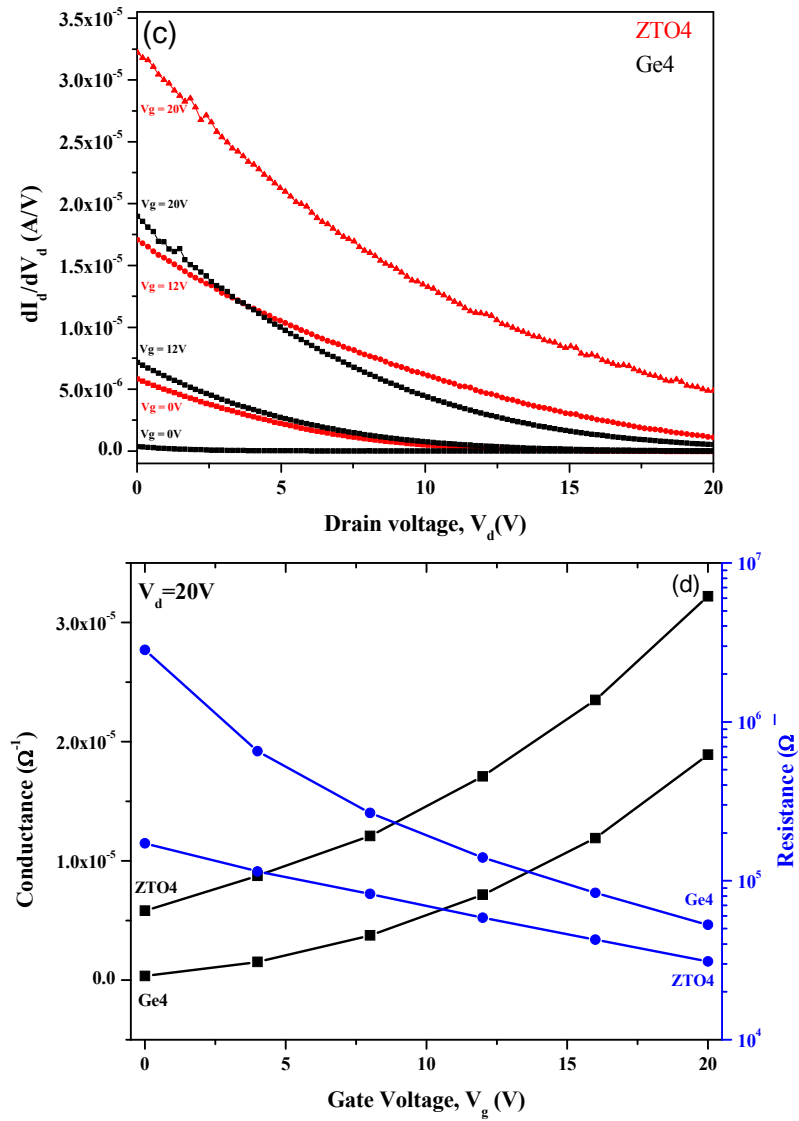
101

Fig. 4.12 (a) Transfer characteristics (I_d *vs* V_g for drain voltage, V_d = 20V), (b) output characteristics (I_d *vs* V_d for various gate voltages), (c) differential conductance of output characteristics as a function of V_d and (d) total resistance, R_T between source and drain and conductance, C_T as a function of V_g for the ZTO4 and Ge4-TFTs.
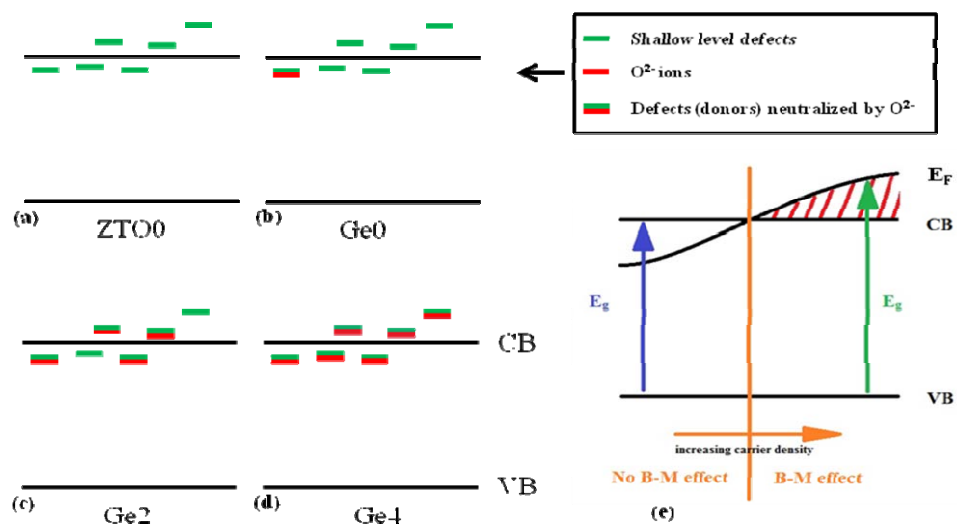
102

Fig. 4.13 Schematic energy band diagram of (a) ZTO0, (b) Ge0, (c) Ge2, (d) Ge4 showing the effect of increase in O^{2-} concentration on shallow defects and (e) role of carrier density on the shift of Fermi level (E_F) and band-gap in B-M effect .

Table 4.3

Device parameters including μ_{Sat}, μ_{linear}, V_{th}, SS, I_{on}/I_{off} ratio, R_{S-D}, N_{SS}, and D_{it} for the ZTO4 and Ge4-TFTs.

	ZTO4	Ge4
μ_{Sat}, (cm^2/Vs)	6.47	5.29
μ_{linear}, (cm^2/Vs)	4	3.36
SS, (V/dec)	2.22	1.39
V_{th}, (V)	-4	+5
I_{on}/I_{off}, (Ratio)	4×10^4	2.5×10^6
R_{S-D}, (Ω)	5.1×10^5	9.8×10^5
N_{SS}, $(eV^{-1}cm^{-3})$	1.07×10^{19}	7.047×10^{18}
D_{it}, $(eV^{-1}cm^{-2})$	5.356×10^{11}	3.52×10^{11}

Table 4.4

Chemical composition obtained from XP spectra for the Ge-doped ZTO and ZTO films.

	Zn/[Sn +Zn+Ge] (at%)	Sn/[Sn +Zn+Ge] (at%)	Ge/[Sn +Zn+Ge] (at%)
.			
ZTO0	40.61	59.39	0
ZTO2	39.41	60.59	0
ZTO4	39.61	60.39	0
Ge0	56.98	42.82	0.19
Ge2	62.29	37.49	0.21
Ge4	65.71	34.10	0.18

Publications

Papers (SCI Journals)

[1] <u>Abhishek Sharma</u> and S.-I. Yoo, "Subsolidus phase relationships in the Al_2O_3–SnO_2–ZnO ternary system at 1200ºC in air", *Journal of Alloys and Compounds*, 740 (2018) 536-540.

[2] <u>Abhishek Sharma</u>, Dami Kim and S.-I. Yoo, "Subsolidus phase diagram in the GeO_2–ZnO–SnO_2 system at 1100ºC in air", *submitted to Ceramics International*.

[3] <u>Abhishek Sharma</u>, Rahim Abdur, Dami Kim, Awnish Kumar Tripathi, Son Singh, Jaegab Lee and Sang-Im Yoo, "Enhancement in structural-electrical-optical properties and TFT performance of Zn-Sn-O based thin films by Ge doping", *to be submitted*.

[4] <u>Abhishek Sharma</u>, Rahim Abdur, Dami Kim, Son Singh, Jaegab Lee and Sang-Im Yoo, "A review on Al-doped Zn-Sn-O based amorphous thin film transistors", *in preparation*.